

A TWO-DIMENSIONAL STABILIZED DISCONTINUOUS GALERKIN METHOD ON CURVILINEAR EMBEDDED BOUNDARY GRIDS

ANDREW GIULIANI*

Abstract. In this work, we propose a state redistribution method for high order discontinuous Galerkin methods on curvilinear embedded boundary grids. State redistribution relaxes the overly restrictive CFL condition that results from arbitrarily small cut cells when explicit time steppers are used. Thus, the scheme can take time steps that are proportional to the size of cells in the background grid. The discontinuous Galerkin scheme is stabilized by postprocessing the numerical solution after each stage or step of an explicit time stepping method. This is done by temporarily coarsening, or merging, the small cells into larger, possibly overlapping neighborhoods using a special weighted inner product. Then, the numerical solution on the neighborhoods is refined back onto the base grid in a conservative fashion. The advantage of this approach is that it uses only basic mesh information that is already available in many cut cell codes and does not require complex geometric manipulations. We prove that state redistribution is conservative and p -exact. Finally, we solve a number of test problems that demonstrate the encouraging potential of this technique for applications on curvilinear embedded geometries. Numerical experiments reveal that our scheme converges with order $p + 1$ in L_1 and between p and $p + 1$ in L_∞ .

Key words. state redistribution, discontinuous Galerkin methods, cut cell grids, explicit time stepping, curvilinear embedded boundaries.

AMS subject classifications. 65M60, 65M20, 35L02, 35L65

1. Introduction. Practical problems in computational fluid dynamics require the solution of hyperbolic conservation laws on complex domains. Typically, the domain is first discretized into a mesh of elements, then algorithms such as the finite volume (FV) or discontinuous Galerkin (DG) methods are used to approximate the exact solution on that mesh. When the boundary of the domain is complex, e.g., an aircraft, the most time-consuming aspect of the workflow can be the mesh generation phase [1]. One technique that solves this problem is the use of embedded-boundary grids whereby the complex boundary is superimposed on a Cartesian grid. The computational mesh is then composed of Cartesian cells on the domain interior and irregular “cut” cells on the domain boundary. These mesh generation algorithms are robust and automated.

A problem that arises when using explicit time stepping methods on embedded boundary grids is the small cell problem. Explicit methods require a time step that is proportional to the cell size in the mesh. Since irregular cut cells on the domain boundary can be arbitrarily small, this results in an overly stiff system of ordinary differential equations that would require impractically small time steps. A special treatment of these cut cells is therefore necessary for explicit time integrators to be used.

Many solutions to the small cell problem in finite volume methods have been proposed, such as flux redistribution [2], h -box methods [3, 4], implicit/explicit time stepping [5, 6], dimensionally-split flux stabilization [7, 8], cell merging [9, 10], and more recently state redistribution (SRD) [11]. Flux redistribution is an approach where each cell is updated with a locally stable, but possibly nonconservative, time step [2]. Excess flux is then locally redistributed in order to maintain conservation. This is straightforward to implement in three dimensions, but is only first order accurate at the embedded boundary. H -box methods are second order accurate, stable, and have desirable theoretical properties [3, 4]. This is achieved by increasing the domain of dependence of fluxes on cut cells, however, doing so in three dimensions seems difficult to implement. Implicit/explicit time integration schemes have also been developed, where the small cells are integrated implicitly and the large cells are integrated explicitly [6]. Finally, cell merging is popular in two dimensions [9, 10]. However, similar to h -box methods, this technique suffers from implementation difficulties in three dimensions due to the many different, possibly incompatible ways to create merging neighborhoods.

Similar approaches have been applied to cut cell DG discretizations. Cell merging [12, 13, 14, 15], subcycling in time [13], and penalization terms [16] have been used to deal with the small cells. When

*Courant Institute, New York University, 251 Mercer St., New York, NY 10012 (giuliani@cims.nyu.edu)

strong anisotropic refinement is required, triangular cut cell approaches for the Navier-Stokes equations have also been examined in [17, 18]. Our approach to the small cell problem is a modification of the state redistribution method, which has been successfully applied to second order finite volume methods in two dimensions [11]. The idea behind state redistribution is to temporarily merge cut cells into larger, possibly overlapping neighborhoods in a postprocessing step applied after each explicit time step. For finite volume schemes, the spatial accuracy of state redistribution is increased by reconstructing a polynomial on each merging neighborhood. Then, these neighborhood polynomials are recombined in a conservative manner back onto the base grid. Applying state redistribution to DG numerical solutions follows a similar strategy, however, since the DG scheme does not rely on reconstructions, there are notable differences. Specifically, the DG numerical solution is composed of discontinuous, locally defined polynomials that are written as linear combinations of polynomial basis functions. Thus, we adapt our state redistribution approach to DG methods by associating to each possibly overlapping, merging neighborhood a tailored polynomial basis. The DG solution is projected onto these overlapping merging neighborhoods using a particular weighted inner product. Then, the numerical solution is projected back onto basis functions defined on elements of the embedded boundary grid. The state redistribution method for finite volume methods is an attractive technique as it only requires mesh information that is already available in many cut cell codes: the geometry of the cut cell, and its connectivity information. There are two additional requirements for DG methods: (1) the ability to compute inner products on the cut cells, and (2) basis functions on the cut cells and neighborhoods. In this work, we will describe both the DG scheme on the base cut cell grid and how to relax the time step restriction on cut cell grids using state redistribution. Typically, numerical schemes on embedded boundary grids suffer from a loss of accuracy at the boundary, due to the irregularity of the grid and we will examine this on a number of numerical examples.

The structure of this article is as follows. In section 2 we briefly describe the spatial discretization used to approximate solutions to hyperbolic conservation laws. In section 3, we recall the state redistribution method for finite volume schemes and outline how to extend it to arbitrarily high order discontinuous Galerkin methods. This will involve the projections that we discussed previously. For ease of understanding and to reduce the necessary notation, this section uses a model problem in one space dimension. In sections 4 and 5, we go into more detail for two-dimensional computations. In section 6, we show that the approach is p -exact and also conservative. In section 7, we present a number of numerical experiments. In particular, we examine the error at cut cells, confirming the results in [12, 16] that the cut cell methods suffer some loss of accuracy at the boundary.

2. The discontinuous Galerkin method on cut cell meshes. We aim to approximate solutions to hyperbolic conservation laws

$$(2.1) \quad \mathbf{u}_t + \nabla \cdot \mathbf{F}(\mathbf{u}) = 0 \quad \text{on } \Omega \times (0, T),$$

using the discontinuous Galerkin method coupled with explicit time steppers on cut cell meshes. In the above, $\Omega \subset \mathbb{R}^2$ is the spatial domain, T is the final time, $\mathbf{u} : \Omega \times (0, T) \rightarrow \mathbb{R}^m$, $m \in \mathbb{N}$ is a vector of conserved quantities and \mathbf{F} is a flux function.

2.1. Mesh generation. The domain Ω is discretized with a mesh of elements $K_{i,j}$, by superimposing the boundary of $\partial\Omega$ on a Cartesian grid and deleting the solid portions of the grid. The geometry in two dimensions is defined as a function that takes a point (x, y) and returns whether it's inside or outside the domain. In the volume, the mesh comprises regular Cartesian cells of dimension Δx by Δy . On the boundary, there are irregular polygons with both straight and curved edges that are determined by the intersections of the boundary, $\partial\Omega$, with the Cartesian grid. The x and y coordinates of the curved edge are polynomials of degree q that interpolate $\partial\Omega$ at $q + 1$ points. For example, the cut cell on the right in Figure 2.1 has one curved edge, where $q = 2$. As it is shown in [19], discontinuous Galerkin methods require at least piecewise quadratic approximations to curved boundaries. Thus, we always pair the second order DG method ($p = 1$) with a piecewise quadratic approximation of the boundary ($q = 2$). Otherwise, we let $p = q$ when $p > 1$. Each cut cell is assumed to have at most two, possibly

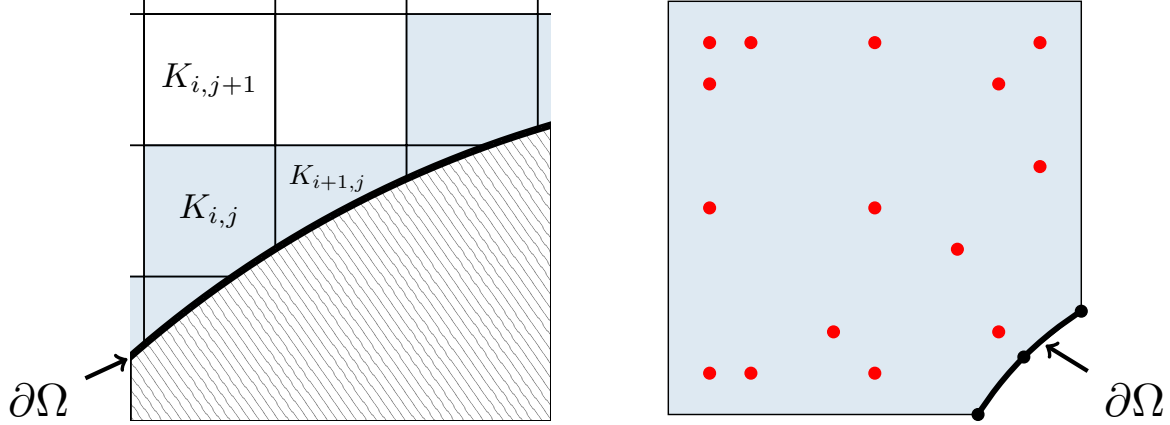


FIG. 2.1. On the left, we plot a zoom of a curvilinear cut cell grid at the boundary, where whole cells are white and cut cells are light blue. The boundary of the domain $\partial\Omega$ is the bold black line. On the right, we show the quadrature rule for $p = 2$ of degree 4 on $K_{i,j}$. There are $N_{i,j}^{vol} + 1 = 15$ quadrature points on this cell. The intersection of the cell with the embedded boundary are indicated by black circles (\bullet) and the volume quadrature points of the cut cell are red circles (\bullet).

curved, irregular edges associated to the embedded boundary ($\partial\Omega$). For example, the cut cells in Figure 2.1 (highlighted in blue), only have one irregular edge. Cells that have two irregular edges lie on sharp corners of the embedded boundary (Figure 7.3). We also do not allow split or tunneled cells for ease of code development. This restriction is not fundamental and we will need to implement these features in three dimensions for complicated geometries. We have made our mesh generation code written in Python available at <https://github.com/andrewgiuliani/PyGrid-2D>. This code can be used to reproduce all the high order embedded boundary grids used in this work, as well as generate other embedded boundary grids in two dimensions.

2.2. Semidiscretization. We use the modal discontinuous Galerkin method as the base scheme on this cut cell grid. Multiplying (2.1) by a test function $v(x, y) \in H^1(K_{i,j})$ and integrating on cell $K_{i,j}$, we obtain

$$\int_{K_{i,j}} \mathbf{u}_t v \, dx \, dy + \int_{K_{i,j}} \nabla \cdot \mathbf{F}(\mathbf{u}) v \, dx \, dy = 0 \quad \forall v \in H^1(K_{i,j}).$$

Integrating the second term by parts and using the divergence theorem, we have

$$\int_{K_{i,j}} \mathbf{u}_t v \, dx \, dy + \int_{\partial K_{i,j}} v \mathbf{F}(\mathbf{u}) \cdot \mathbf{n} \, dl - \int_{K_{i,j}} \mathbf{F}(\mathbf{u}) \cdot \nabla v \, dx \, dy = 0 \quad \forall v \in H^1(K_{i,j}).$$

The solution \mathbf{u} and test function v are then restricted to $S^p(K_{i,j})$, the space of polynomials of degree less than or equal to p on $K_{i,j}$. On each cell, Cartesian and cut, we use a non-tensor product, orthonormal basis for $S^p(K_{i,j})$ that has $N_p + 1$ basis functions, where $N_p = (p + 1)(p + 2)/2 - 1$. Alternatively, a tensor product basis [12] can be used. Tensor and non-tensor product bases have respectively $(p + 1)^2$ and $(p + 1)(p + 2)/2$ basis functions. We prefer a non-tensor product basis (section 4.2) due to the computational savings that result from a smaller set of basis functions. The numerical solution on each cell is written

$$(2.2) \quad \mathbf{U}_{i,j}(x, y, t) = \sum_{k=0}^{N_p} \mathbf{c}_{i,j,k}(t) \varphi_{i,j,k}(x, y),$$

where $\mathbf{c}_{i,j,k} \in \mathbb{R}^m$ is the k th solution coefficient associated to basis function $\varphi_{i,j,k}$ on cell $K_{i,j}$, where the $\varphi_{i,j,k}$ are orthonormal with respect to the inner product

$$(2.3) \quad \langle f, g \rangle_{K_{i,j}} = \frac{1}{|K_{i,j}|} \int_{K_{i,j}} f g \, dx \, dy,$$

where $|K_{i,j}|$ is the volume of cell i, j . The modal discontinuous Galerkin method is then given by the system of ordinary differential equations

$$(2.4) \quad \frac{d}{dt} \mathbf{c}_{i,j,k} = -\frac{1}{|K_{i,j}|} \left[\int_{\partial K_{i,j}} \varphi_{i,j,k} \mathbf{F}^*(\mathbf{U}_{i,j}^-, \mathbf{U}_{i,j}^+) \cdot \mathbf{n} \, dl - \int_{K_{i,j}} \mathbf{F}(\mathbf{U}_{i,j}) \cdot \nabla \varphi_{i,j,k} \, dx \, dy \right],$$

for $k = 0, \dots, N_p$, where $\mathbf{U}_{i,j}^-$ and $\mathbf{U}_{i,j}^+$ are the numerical solutions corresponding to $K_{i,j}$, and a neighboring cell, respectively, located along the element boundary $\partial K_{i,j}$. Finally, \mathbf{n} is an outward facing unit normal, and \mathbf{F}^* is a numerical flux function.

The semidiscretization (2.4) is integrated in time using a $(p+1)$ th order accurate Runge Kutta time stepping algorithm. Since the cut cell grid can contain arbitrarily small cut cells, (2.4) can be stiff, and be subject to an arbitrarily small time step restriction. State redistribution will allow the use of explicit time stepping algorithms on cut cell grids with a time step that is proportional to the Cartesian cell size

$$(2.5) \quad \Delta t \left(\frac{|a|}{\Delta x} + \frac{|b|}{\Delta y} \right) \leq \frac{1}{2p+1},$$

where $|a|, |b|$ are the maximum wave speeds in the x and y directions [20, 21].

The DG method above requires an orthogonal polynomial basis on each polygonal cut cell. We numerically compute orthogonal basis functions and their gradients at quadrature points using the QR factorization of a Vandermonde-like matrix (section 4.2).

2.3. Quadrature on curved polygons. One issue with cut cell DG approaches that arises independently of the small cell problem is the evaluation of inner products on arbitrary curved polygons. Quadrature rules are required to approximate volume integrals on elements

$$\int_{K_{i,j}} f(x, y) g(x, y) \, dx \, dy \approx \sum_{q=0}^{N_{i,j}^{\text{vol}}} w_{i,j,q} f(x_{i,j,q}, y_{i,j,q}) g(x_{i,j,q}, y_{i,j,q}),$$

where $N_{i,j}^{\text{vol}} + 1$ is the number of volume quadrature points on $K_{i,j}$, and $\sum_{q=0}^{N_{i,j}^{\text{vol}}} w_{i,j,q} = |K_{i,j}|$. Some approaches are based on the divergence theorem [22], hierarchical moment fitting [23, 24], “speckling” of quadrature points [17, 18], and others [25, 26]. We use the software described in [27, 28] for quadrature rules on polygons with curved edges, but other quadrature generation codes can be used as well. By construction, this algorithm always results in quadrature nodes interior to the polygon with positive weights. Another well-known approach is to triangulate the polygon and apply standard quadrature rules on each subtriangle [12]. Typically, this algorithm results in too many quadrature points and weights and does not generalize to three dimensions since not all polyhedra can be triangulated without introducing vertices. Finally, quadrature by triangulation can also be difficult to robustly use with curvilinear embedded boundaries. Initially, our code used this technique by triangulating the cut cells in such a way that only one triangle had a curved edge. Then, we applied quadrature rules on both curved and straight-edge triangles by mapping them to a canonical triangle. We did not find a satisfactory technique to guarantee an invertible mapping from curved to canonical triangles, and so abandoned obtaining quadrature rules by triangulation.

On all elements, both whole and cut, we use quadrature rules of degree $2p$. Surface integrals are approximated using standard Gauss-Legendre rules of degree $2p+1$, with $p+1$ points.

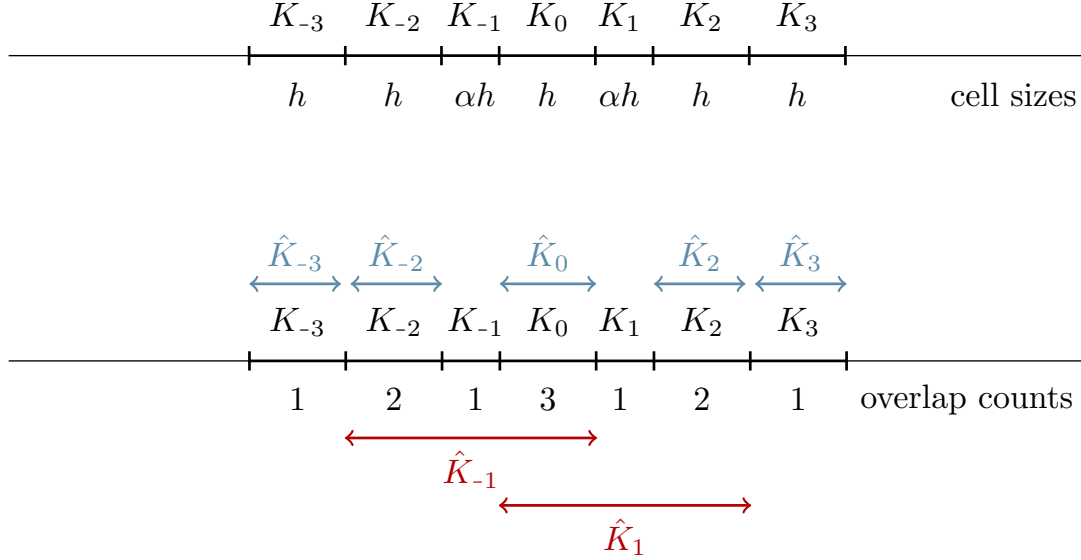


FIG. 3.1. Nonuniform grid for model problem used to describe the state redistribution method for both finite volume and discontinuous Galerkin methods in Section 3. The top figure indicates the cell sizes. The bottom figure shows the merging neighborhoods and the overlap counts on each cell in the base grid. \hat{K}_i refers to the merging neighborhood associated to cell K_i in the base grid. Neighborhoods that contain only one cell in the base grid are drawn in blue, while those that contain multiple, temporarily merged cells are drawn in red.

3. State redistribution in one dimension. In this section, we demonstrate state redistribution with a simple example that solves the linear advection equation

$$(3.1) \quad u_t + au_x = 0, \quad a > 0$$

on the nonuniform grid in Figure 3.1, called the base grid. On full cells, $h_i = h$ and on the small cells, $h_i = \alpha h$ for $0 < \alpha < 1$. Five cells (indexed by $-3, -2, 0, 2, 3$) are large with size h and the remaining two cells (indexed by -1 and 1) are small with size αh . For completeness, we first recall how to stabilize a first order upwind finite volume scheme using the approach described in [11]. Note that this scheme can be viewed as a discontinuous Galerkin method when $p = 0$. Then, we will describe how to extend this approach to arbitrarily high order discontinuous Galerkin methods.

State redistribution with finite volume methods. We discretize (3.1) using the first order, upwind finite volume scheme

$$(3.2) \quad \hat{U}_i = U_i^n - \frac{a\Delta t}{h_i}(U_i^n - U_{i-1}^n).$$

To apply state redistribution to the above finite volume scheme, we must execute a simple geometric preprocessing stage on the grid before the iterative portion of the finite volume solver.

During this preprocessing stage, we associate a merging neighborhood \hat{K}_i to each cell in the base grid, K_i . Cells that are smaller than half the regular grid size ($h_i < h/2$), are merged to the left and right to form the merging neighborhoods $\hat{K}_{-1} = K_{-2} \cup K_{-1} \cup K_0$ and $\hat{K}_1 = K_0 \cup K_1 \cup K_2$ (Figure 3.1, in red). Cells that are larger than half the regular grid size ($h_i \geq h/2$) do not require merging and we have $\hat{K}_i = K_i$ (Figure 3.1, in blue). Additionally, each cell in the base grid must count the number of neighborhoods that overlap it, N_i . For example, since K_0 is a member of three neighborhoods: \hat{K}_{-1} , \hat{K}_0 , and \hat{K}_1 , its overlap count is $N_0 = 3$. We have provided the overlap counts for the cells on the base grid in Figure 3.1.

After the preprocessing stage has been completed, we apply state redistribution as a postprocessing step after each forward Euler update of (3.2). On each neighborhood, we compute a special weighted solution average. For example, on \hat{K}_{-1} the weighted solution average is

$$(3.3) \quad \hat{Q}_{-1} = \frac{1}{h/2 + \alpha h + h/3} \left(\frac{h}{2} \hat{U}_{-2} + \alpha h \hat{U}_{-1} + \frac{h}{3} \hat{U}_0 \right),$$

where both cell size and solution average in the above sums are divided by their associated overlap counts. Similarly, on \hat{K}_1 the weighted solution average is

$$\hat{Q}_1 = \frac{1}{h/2 + \alpha h + h/3} \left(\frac{h}{2} \hat{U}_2 + \alpha h \hat{U}_1 + \frac{h}{3} \hat{U}_0 \right).$$

On neighborhoods that only contain one cell, the weighted solution average is

$$\hat{Q}_i = \hat{U}_i \text{ for } i = -3, -2, 0, 2, 3.$$

Finally, these weighted solution averages are recombined back onto the base grid. The final update of a cell in the base grid is given by the average of the neighborhood values that overlap it. For example, since K_0 is overlapped by \hat{K}_{-1} , \hat{K}_0 , and \hat{K}_1 , we have

$$(3.4) \quad U_0^{n+1} = \frac{1}{3}(\hat{Q}_{-1} + \hat{Q}_0 + \hat{Q}_1).$$

K_{-2} and K_2 are overlapped by two neighborhoods, so their final updates are

$$(3.5) \quad U_{-2}^{n+1} = \frac{1}{2}(\hat{Q}_{-2} + \hat{Q}_{-1}) \text{ and } U_2^{n+1} = \frac{1}{2}(\hat{Q}_2 + \hat{Q}_1).$$

On the cells overlapped by only one neighborhood, the final update is simply

$$(3.6) \quad U_i^{n+1} = \hat{Q}_i \text{ for } i = -3, -1, 1, 3.$$

We prove in [11] that the above scheme in (3.4)-(3.6), is conservative. Additionally, we show that it can be extended to second order FV methods by reconstructing a slope on each merging neighborhood and using that slope to recombine the neighborhood averages back onto the base grid in a linearity preserving fashion. In the following section, we describe how to extend this idea to discontinuous Galerkin methods.

State redistribution with discontinuous Galerkin methods. We discretize (3.1) in space using an upwind RK-DG scheme where the degree of the polynomial approximation is p . Assuming an SSP-RK scheme, the first forward Euler update can be written

$$(3.7) \quad \hat{c}_{i,k} = c_{i,k}^n - \frac{a\Delta t}{h_i} \left[U_i^n(x_{i+1/2})\varphi_{i,k}(x_{i+1/2}) - U_{i-1}^n(x_{i-1/2})\varphi_{i,k}(x_{i-1/2}) - \int_{K_i} U_i^n \varphi'_{i,k} dx \right], \text{ for } k = 0 \dots p,$$

where $\hat{c}_{i,k}$ are the provisionally updated solution coefficients, U_i^n is the DG solution on cell K_i at time t^n and \hat{U}_i is its provisionally updated (possibly unstable) counterpart

$$U_i^n(x) = \sum_{k=0}^{N_p} c_{i,k}^n \varphi_{i,k}(x), \quad \hat{U}_i(x) = \sum_{k=0}^{N_p} \hat{c}_{i,k} \varphi_{i,k}(x).$$

Additionally, the time step is $\Delta t = ah/(2p+1)$ on all cells, and $\varphi_{i,k}$ are the orthonormal basis functions of $S^p(K_i)$ with respect to the inner product in (2.3).

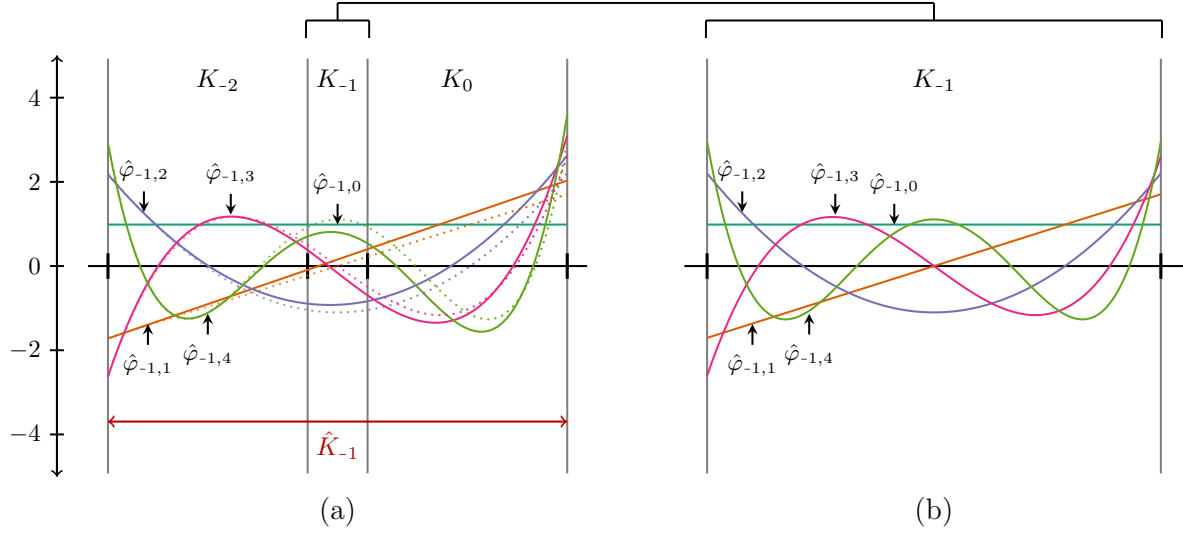


FIG. 3.2. In a), we plot the basis functions (solid lines) that are orthogonal with respect to the weighted inner product $\langle \cdot, \cdot \rangle_{\hat{K}_{-1}}$ in (3.8). Although the basis functions in a) appear to be translations and rescaling of the standard Legendre polynomials, a closer inspection reveals that they are not. We have plotted the normalized Legendre polynomials (dotted lines) on the same axes to illustrate the difference. In b), we plot the orthogonal basis functions with respect to $\langle \cdot, \cdot \rangle_{K_{-1}}$, which are simply translations and rescaling of the standard Legendre polynomials. Note that functions in b) are plotted on element K_{-1} , which is the center element in a).

Similar to the SRD stabilized FV scheme described earlier, we must complete a preprocessing stage, whereby merging neighborhoods are associated to each cell in the base grid. For the illustration here, we use the same merging neighborhoods as in the finite volume example. The postprocessing stage described below is more involved for the DG scheme due to the spatial accuracy required and comprises two projections:

1. The first step projects the provisionally updated numerical solution from the base grid, \hat{U}_i , onto basis functions defined on merging neighborhoods. They are called, $\hat{\varphi}_{i,k}$ and they span $S^p(\hat{K}_i)$.
2. The second step projects the numerical solution from the merging neighborhoods back onto the basis functions defined on the base grid. They are called $\varphi_{i,k}$, and they span $S^p(K_i)$.

We emphasize that the neighborhood basis functions are not generally the same basis functions as the ones on the base grid. In this example, $\varphi_{i,k}$ and $\hat{\varphi}_{i,k}$ are not identical, and are defined on different domains. Specifically, the basis functions on the base grid $\varphi_{i,k}$ are orthogonal with respect to the inner product in (2.3). In contrast, the basis functions defined on the merging neighborhoods $\hat{\varphi}_{i,k}$ are orthogonal with respect to a particular weighted L_2 inner product. For example, $\hat{\varphi}_{-1,k}$ is the k th orthonormal basis function of $S^p(\hat{K}_{-1})$ with respect to the inner product

$$(3.8) \quad \langle f, g \rangle_{\hat{K}_{-1}} = \frac{1}{h/2 + \alpha h + h/3} \left(\frac{1}{2} \int_{K_{-2}} f g \, dx + \int_{K_{-1}} f g \, dx + \frac{1}{3} \int_{K_0} f g \, dx \right).$$

Note that in the above inner product, the cell sizes are divided by their associated overlap counts. Additionally, each integral is divided by the overlap count associated to its domain of integration: the first integral is divided by two since $N_{-2} = 2$, the second integral is divided by one since $N_{-1} = 1$, and the final integral is divided by three since $N_0 = 3$. In Figure 3.2, we plot both $\varphi_{-1,k}$ and $\hat{\varphi}_{-1,k}$ for $k = 0, 1, \dots, 4$ and make two observations. First, $\varphi_{-1,k}$ and $\hat{\varphi}_{-1,k}$ are defined on different domains. Second, the basis functions $\varphi_{-1,k}$ on the base grid are simply translations and rescalings of the Legendre polynomials, as expected, while the neighborhood basis functions $\hat{\varphi}_{-1,k}$ are not.

We are now ready to compute the projection $\hat{Q}_{-1}(x)$ of the provisionally updated DG solutions, \hat{U}_{-2} , \hat{U}_{-1} , \hat{U}_0 , onto the merging basis for \hat{K}_{-1} :

$$(3.9) \quad \hat{Q}_{-1}(x) = \sum_{k=0}^{N_p} \hat{q}_{i,k} \hat{\varphi}_{-1,k}.$$

Due to the orthogonality of the basis functions, the coefficients $\hat{q}_{i,k}$ are written

$$(3.10) \quad \hat{q}_{-1,k} = \frac{1}{h/2 + \alpha h + h/3} \left(\frac{1}{2} \int_{K_{-2}} \hat{U}_{-2} \hat{\varphi}_{-1,k} dx + \int_{K_{-1}} \hat{U}_{-1} \hat{\varphi}_{-1,k} dx + \frac{1}{3} \int_{K_0} \hat{U}_0 \hat{\varphi}_{-1,k} dx \right) \text{ for } k = 0 \dots p,$$

This operation can be viewed as a local coarsening of the provisionally updated DG solution from the cells K_{-2} , K_{-1} , K_0 onto the merging neighborhood \hat{K}_{-1} . Due to the projection operation, $\hat{Q}_{-1}(x)$ defined in (3.9) is the closest polynomial of degree p to the piecewise defined provisionally updated solution, \hat{U}_{-2} , \hat{U}_{-1} , and \hat{U}_0 on \hat{K}_{-1} , measured in the weighted norm $\sqrt{\langle \cdot, \cdot \rangle_{\hat{K}_{-1}}}$ that follows from (3.8). Also, note that formula (3.10) is a generalization of the finite volume formula in (3.3), and simplifies to (3.3) when $p = 0$ since the provisional solution updates \hat{U}_{-2} , \hat{U}_{-1} , \hat{U}_0 are constants for finite volume methods. In contrast, they are polynomials for the DG method in (3.10).

Each merging neighborhood has its own weighted inner product, which depends on how cells are merged and their associated overlap counts. For example, $\hat{\varphi}_{1,k}$ is the k th orthonormal basis function of $S^p(\hat{K}_1)$ with respect to the weighted L_2 inner product

$$\langle f, g \rangle_{\hat{K}_1} = \frac{1}{h/2 + \alpha h + h/3} \left(\frac{1}{2} \int_{K_2} f g dx + \int_{K_1} f g dx + \frac{1}{3} \int_{K_0} f g dx \right),$$

where again the cell sizes and integrals are divided by their associated overlap counts. Additionally, the solution coefficients of the projected solution on \hat{K}_1 are written

$$\hat{q}_{1,k} = \frac{1}{h/2 + \alpha h + h/3} \left(\frac{1}{2} \int_{K_2} \hat{U}_2 \hat{\varphi}_{1,k} dx + \int_{K_1} \hat{U}_1 \hat{\varphi}_{1,k} dx + \frac{1}{3} \int_{K_0} \hat{U}_0 \hat{\varphi}_{1,k} dx \right).$$

The merging neighborhood associated to large cells contain only one cell of the base grid. The inner product on such cell, e.g., \hat{K}_0 is

$$\begin{aligned} \langle f, g \rangle_{\hat{K}_0} &= \frac{1}{h_0/3} \left(\frac{1}{3} \int_{K_0} f g dx \right) \\ &= \frac{1}{h_0} \int_{K_0} f g dx, \end{aligned}$$

where again we divide the cell volume and integral by their associated overlap counts. However, notice that the overlap counts cancel out and the inner product simplifies. We can make the more general statement that on the neighborhoods that contain only one cell of the base grid, we have $\langle f, g \rangle_{\hat{K}_i} = \langle f, g \rangle_{K_i}$ since

$$\begin{aligned} \langle f, g \rangle_{\hat{K}_i} &= \frac{1}{h_i/N_i} \left(\frac{1}{N_i} \int_{K_i} f g dx \right) \\ &= \frac{1}{h_i} \int_{K_i} f g dx \\ &= \langle f, g \rangle_{K_i}, \text{ for } i = -3, -2, 0, 2, 3. \end{aligned}$$

due to cancellation of the overlap counts. Thus, the solution coefficients of the numerical solution on the merging neighborhoods associated to large cells in the base grid are

$$\begin{aligned}\hat{q}_{i,k} &= \frac{1}{h_i} \left(\int_{\hat{K}_i} \hat{U}_i \hat{\varphi}_{i,k} dx \right) \\ &= \hat{c}_{i,k}\end{aligned}$$

since $\hat{K}_i = K_i$ and the neighborhood inner product is the same as the base grid inner product. This implies that $\hat{\varphi}_{i,k} = \varphi_{i,k}$ for $k = 0 \dots p$ and $i = -3, -2, 0, 2, 3$. In other words, preprocessing is only required in the neighborhood of cut cells.

The final step is to project the stabilized neighborhood polynomials from the merging neighborhoods, \hat{Q}_i , back onto the base grid. For a given cell, K_i , in the base grid, we can average the stabilized neighborhood polynomials that overlap it and then project that average onto the base grid basis functions $\varphi_{i,k}$ associated to K_i . For example, K_0 is overlapped by three merging neighborhoods: \hat{K}_{-1} , \hat{K}_0 , \hat{K}_1 . Therefore, the stabilized solution coefficients on K_0 after one stage of the SSP-RK method are written

$$c_{0,k}^{n+1} = \frac{1}{h_0} \int_{K_0} \frac{1}{3} (\hat{Q}_{-1} + \hat{Q}_0 + \hat{Q}_1) \varphi_{0,k} dx, \text{ for } k = 0 \dots p.$$

The solution coefficients on cells overlapped by two merging neighborhoods, K_{-2} and K_2 , can be written

$$(3.11) \quad c_{-2,k}^{n+1} = \frac{1}{h_{-2}} \int_{K_{-2}} \frac{1}{2} (\hat{Q}_{-2} + \hat{Q}_{-1}) \varphi_{-2,k} dx, \text{ and } c_{2,k}^{n+1} = \frac{1}{h_2} \int_{K_2} \frac{1}{2} (\hat{Q}_2 + \hat{Q}_1) \varphi_{2,k} dx,$$

for $k = 0 \dots p$. Finally, the solution coefficients on cells overlapped by one merging neighborhood is

$$c_{i,k}^{n+1} = \frac{1}{h_i} \int_{K_i} \hat{Q}_i \varphi_{i,k} dx, \text{ for } k = 0 \dots p, \ i = -3, -1, 1, 3.$$

We will prove in section 6 that state redistribution is p -exact and conservative.

We have just described how to apply state redistribution to a single forward Euler stage of an SSP Runge Kutta method. For non-SSP explicit Runge Kutta methods, state redistribution can be applied to the intermediate and final solutions. In the next section, we will describe the details of the pre- and postprocessing steps of the state redistribution algorithm for the discontinuous Galerkin method in two dimensions.

One-dimensional convergence test: to conclude this section, we solve the linear advection equation

$$(3.12) \quad \begin{aligned} u_t + u_x &= 0 \text{ on } [-1, 1], \\ u(x, 0) &= \sin(\pi x), \end{aligned}$$

with periodic boundary conditions on the nonuniform grid in Figure 3.3c), which is similar to the grid in Figure 3.1. This grid has $2N + 3$ elements where $2N + 1$ cells have size h and the remaining two elements can be arbitrarily small with size αh , where $0 < \alpha < 1$ is a small. On the grid, cell K_0 is centered at $x = 0$ and $h = 2/(2N + 1 + 2\alpha)$ with $\alpha = 10^{-5}$. We solve (3.12) using the DG scheme in (3.7) stabilized by state redistribution, where the time step is

$$(3.13) \quad \Delta t = \frac{0.9}{2p + 1} h$$

on all cells. The L_1 and L_∞ errors at the final time $T = 1$ are provided in Figure 3.3, where we observe the expected $p + 1$ rate of convergence in both norms. Even though there are two cells that are vastly smaller than the ones used to determine the time step in (3.13), state redistribution allows us to explicitly time step in a stable manner. The Python code that generated this convergence study is available at <https://github.com/andrewgiuliani/PyDGSRD-1D>. It can be used with other one-dimensional conservation laws and non-uniform grids.

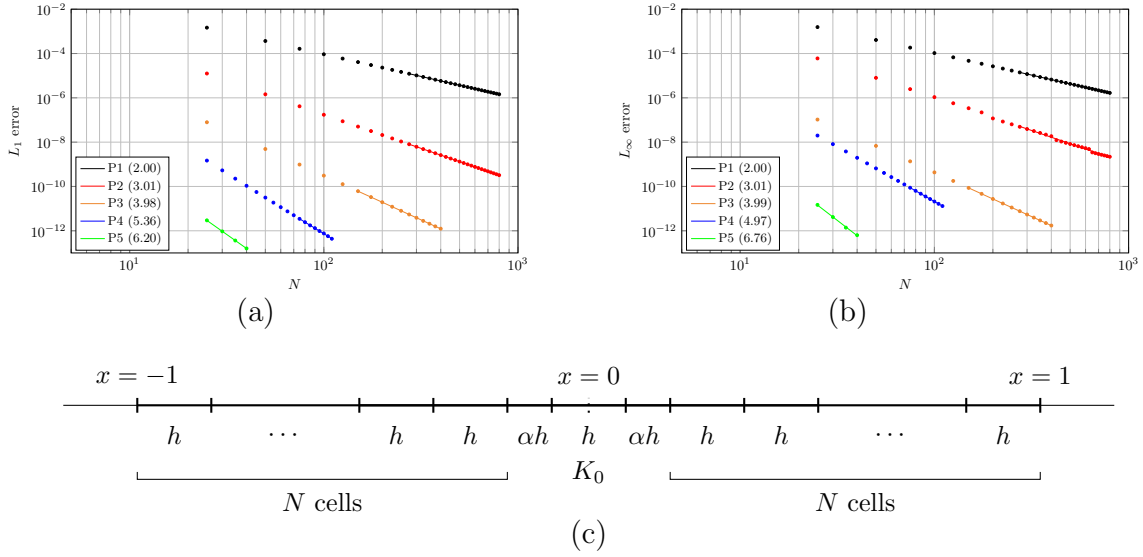


FIG. 3.3. In a) and b), we provide the L_1 and L_∞ errors respectively, at the final time $T = 1$ on the grid shown in c). State redistribution does not affect the rate of convergence at the small cells since we observe the expected $p + 1$ rate of convergence in both the L_1 and L_∞ norms.

4. Preprocessing in two dimensions. In two dimensions, there are three main preprocessing operations. First, merging neighborhoods must be associated to each cell in the cut cells (section 4.1). This operation relies only on mesh information already available in many cut cell codes: cell connectivity and the geometric vertices of cut cells. Then, basis functions must be generated on the base grid (section 4.2), and on the merging neighborhoods (section 4.3). This operation relies on quadrature rules for the evaluation of inner products on arbitrary polygons (section 2.3). Since we have only considered static embedded boundaries in this work, these preprocessing steps are only done once. If moving boundaries are considered, the mesh preprocessing would need to be done every time the boundary is modified.

4.1. Merging neighborhoods. Merging neighborhoods on two-dimensional cut cells grids are generated following the same procedure as described in [11]. Each cell in the base grid, $K_{i,j}$, is associated to a merging neighborhood $\hat{K}_{i,j}$. This merging neighborhood is formed by grouping irregular boundary cells with other nearby cells in the direction closest to the boundary normal. This is done until the neighborhood volume satisfies

$$(4.1) \quad \sum_{(r,s) \in M_{i,j}} |K_{r,s}| \geq \frac{1}{2} \Delta x \Delta y,$$

where $M_{i,j}$ is a set containing the indices of each cell belonging to the merging neighborhood $\hat{K}_{i,j}$. For example, in Figures 4.1a) and b) $M_{i,j} = \{(i,j), (i,j+1)\}$ and $M_{i,j+1} = \{(i,j+1)\}$. In (4.1), the chosen threshold of $\Delta x \Delta y / 2$ is informed by analytical results in [29].

Note that these neighborhoods can overlap and thus a given element in the base grid can belong to multiple neighborhoods. Consider the neighborhood $\hat{K}_{i,j}$ associated to $K_{i,j}$ in Figure 4.1a). The neighborhood is highlighted in green and is generated when $K_{i,j}$ is merged in the direction closest the boundary normal (upward) with $K_{i,j+1}$. In contrast, $K_{i,j+1}$ does not need to merge with any neighboring cells, since it is already large enough and satisfies (4.1). Thus, its merging neighborhood is composed of only itself, $\hat{K}_{i,j+1} = K_{i,j+1}$, and is highlighted in Figure 4.1b). Finally, notice that neighborhoods $\hat{K}_{i,j}$ and $\hat{K}_{i,j+1}$ overlap on cell $K_{i,j+1}$.

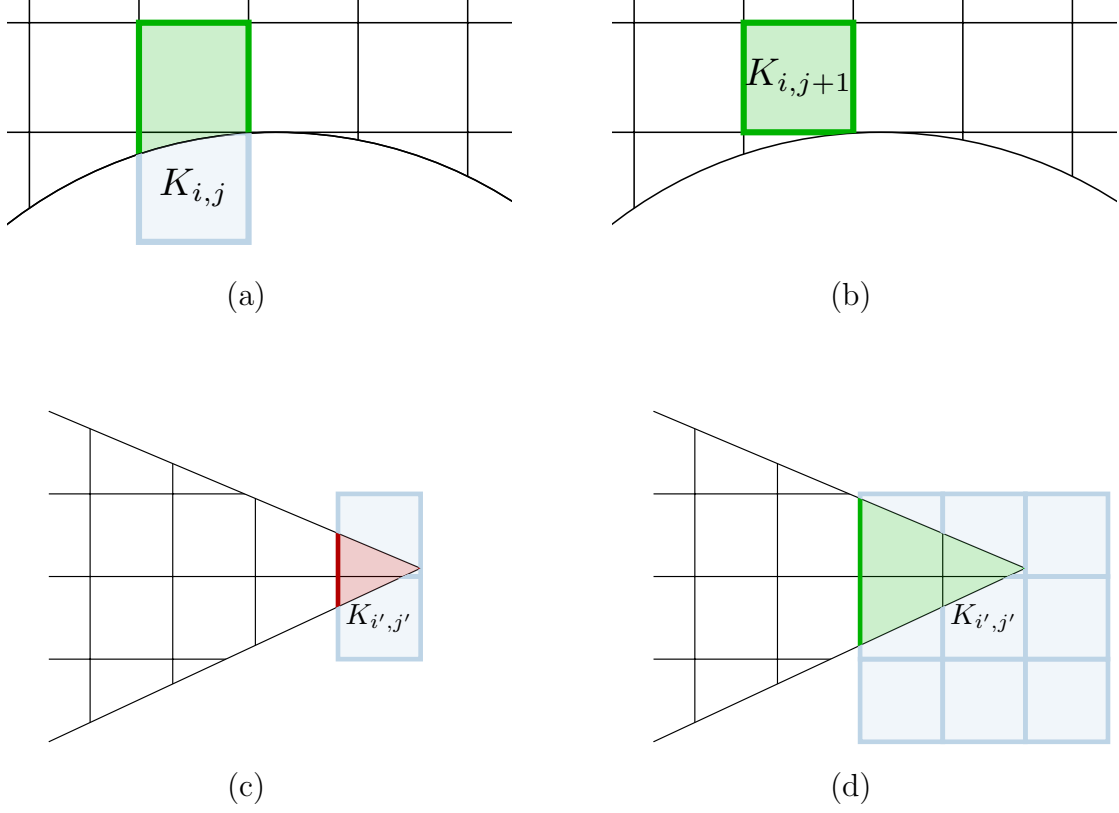


FIG. 4.1. The merging neighborhood of cells $K_{i,j}$ and $K_{i,j+1}$ are highlighted in a) and b), respectively. These neighborhoods overlap on cell $K_{i,j+1}$. The normal merging neighborhood does not always satisfy the volume constraint in (4.1). In c), we show one such neighborhood, associated to $K_{i',j'}$. In d), $K_{i',j'}$ is merged instead with cells on the 3×3 tile centered on $K_{i',j'}$. This alternative approach to merging results in a neighborhood that is large enough. The portions of the grid that are highlighted in blue are solid and do not belong to the computational grid.

For certain boundary configurations, the normal merging neighborhood will not satisfy (4.1). This is shown in Figure 4.1c), for the neighborhood associated to $K_{i',j'}$. In this case, one could merge $K_{i',j'}$ with cells located on the 3×3 tile centered on cell $K_{i',j'}$ (Figure 4.1d), also called the central merging neighborhood.

4.2. Cut cell basis generation. On all cells in the base grid, whole and cut, DG requires a polynomial basis with which to represent the numerical solution.

We prefer to use a basis that is orthogonal with respect to the inner product

$$(4.2) \quad \langle f, g \rangle_{K_{i,j}} = \frac{1}{|K_{i,j}|} \sum_{q=0}^{N_{i,j}^{\text{vol}}} w_{i,j,q} f(x_{i,j,q}, y_{i,j,q}) g(x_{i,j,q}, y_{i,j,q}),$$

a discrete approximation to (2.3). In the above, $w_{i,j,q}$, $x_{i,j,q}$, $y_{i,j,q}$ are the q th volume quadrature weights and points on $K_{i,j}$ (section 2.3). The inner product (4.2) requires the value of the basis functions at the volume and surface quadrature points in order to evaluate the numerical solution in (2.2) for the volume and surface integrals in (2.4). The gradient of the basis functions is also needed at the volume quadrature points for the volume integral in (2.4). This can be done by taking the monomial basis, and applying the modified Gram-Schmidt (MGS) algorithm [30, 31]. A coordinate transformation can also be applied to the initial non-orthogonal monomial basis to reduce the effects of finite precision computations [30].

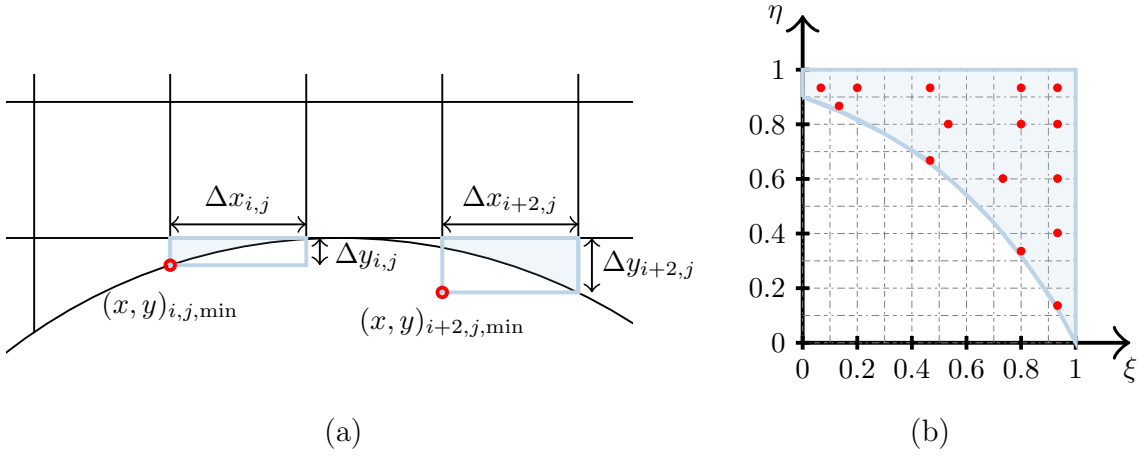


FIG. 4.2. The above figures illustrate how the bounding box of a cut cell is used to generate basis functions. In a), we indicate the bottom left coordinates (•) and dimensions of the bounding box for cells $K_{i,j}$ and $K_{i+2,j}$ used for the basis function calculation on the grid in Figure 4.1a) and b). In b), we plot the points $(\xi, \eta)_{i+2,j,q}$ for $q = 0, 2, \dots$ (indicated by •) at which the basis functions $P_k(\xi, \eta)$ are evaluated to populate the initial Vandermonde-like matrix $V_{i+2,j}$ in (4.4) for element $K_{i+2,j}$.

In this work, we describe another approach, where we determine these basis function values using the QR factorization of a matrix that we describe below.

The matrix that we factorize is based on a Vandermonde-like matrix, populated with the values of initial basis functions that are not necessarily orthogonal with respect (4.2). This initial basis $\{P_k(\xi, \eta)\}_{k=0, \dots, N_p}$ is chosen to span $S^p([0, 1]^2)$ and is orthonormal with respect to the inner product $\langle \cdot, \cdot \rangle_{[0, 1]^2}$. It is generated symbolically using the Gram-Schmidt procedure, using the monomials ordered as $\{1, \xi, \eta, \xi^2, \xi\eta, \eta^2, \dots\}$. The first three of these functions are

$$P_0(\xi, \eta) = 1, \quad P_1(\xi, \eta) = 2\sqrt{3}(\xi - 1/2), \quad P_2(\xi, \eta) = 2\sqrt{3}(\eta - 1/2).$$

Then, we evaluate $P_k(\xi_{i,j,q}, \eta_{i,j,q})$ at each volume quadrature point $(x_{i,j,q}, y_{i,j,q})$ on cell $K_{i,j}$ using the mapping

$$(4.3) \quad (\xi_{i,j,q}, \eta_{i,j,q}) = \left(\frac{x_{i,j,q} - x_{i,j,\min}}{\Delta x_{i,j}}, \frac{y_{i,j,q} - y_{i,j,\min}}{\Delta y_{i,j}} \right),$$

where $(\xi_{i,j,q}, \eta_{i,j,q})$ is the volume quadrature point $(x_{i,j,q}, y_{i,j,q})$ mapped to $[0, 1]^2$, $\Delta x_{i,j}$ is the width of the cell i, j 's bounding box in x direction, and $x_{i,j,\min}$ is the minimum x component of all the vertices of $K_{i,j}$. $\Delta y_{i,j}$ and $y_{i,j,\min}$ are similarly defined in the y direction. These quantities are illustrated in Figure 4.2 for the mesh in Figure 4.1a) and b). Computing the basis function values at the quadrature points uses the QR factorization of a matrix in an oblique inner product [32], and requires three steps:

1. Assemble the initial values of $P_k(\xi_{i,j,q}, \eta_{i,j,q})$ into a Vandermonde-like matrix as follows

$$(4.4) \quad V_{i,j} = \begin{bmatrix} P_0(\xi_{i,j,0}, \eta_{i,j,0}) & P_1(\xi_{i,j,0}, \eta_{i,j,0}) & \dots & P_{N_p}(\xi_{i,j,0}, \eta_{i,j,0}) \\ P_0(\xi_{i,j,1}, \eta_{i,j,1}) & P_1(\xi_{i,j,1}, \eta_{i,j,1}) & \dots & P_{N_p}(\xi_{i,j,1}, \eta_{i,j,1}) \\ \vdots & \vdots & \ddots & \vdots \\ P_0(\xi_{i,j,N_{i,j}^{\text{vol}}}, \eta_{i,j,N_{i,j}^{\text{vol}}}) & P_1(\xi_{i,j,N_{i,j}^{\text{vol}}}, \eta_{i,j,N_{i,j}^{\text{vol}}}) & \dots & P_{N_p}(\xi_{i,j,N_{i,j}^{\text{vol}}}, \eta_{i,j,N_{i,j}^{\text{vol}}}) \end{bmatrix}.$$

2. Multiply the rows of $V_{i,j}$ by the square root of the quadrature weights and using MATLAB we

compute the reduced QR factorization of the product

$$W_{i,j}^{1/2} V_{i,j} = Q_{i,j} R_{i,j},$$

where $W_{i,j} = \text{diag}(w_{i,j,1}, w_{i,j,2}, \dots, w_{i,j,N_{i,j}^{\text{vol}}})$.

3. Compute the product $W_{i,j}^{-1/2} Q_{i,j}$, which contains the orthogonal basis function values at the quadrature points

$$W_{i,j}^{-1/2} Q_{i,j} = \begin{bmatrix} \varphi_{i,j,0}(x_{i,j,0}, y_{i,j,0}) & \varphi_{i,j,1}(x_{i,j,0}, y_{i,j,0}) & \dots & \varphi_{i,j,N_p}(x_{i,j,0}, y_{i,j,0}) \\ \varphi_{i,j,0}(x_{i,j,1}, y_{i,j,1}) & \varphi_{i,j,1}(x_{i,j,1}, y_{i,j,1}) & \dots & \varphi_{i,j,N_p}(x_{i,j,1}, y_{i,j,1}) \\ \vdots & \vdots & \ddots & \vdots \\ \varphi_{i,j,0}(x_{i,j,N_{i,j}^{\text{vol}}}, y_{i,j,N_{i,j}^{\text{vol}}}) & \varphi_{i,j,1}(x_{i,j,N_{i,j}^{\text{vol}}}, y_{i,j,N_{i,j}^{\text{vol}}}) & \dots & \varphi_{i,j,N_p}(x_{i,j,N_{i,j}^{\text{vol}}}, y_{i,j,N_{i,j}^{\text{vol}}}) \end{bmatrix}.$$

The mass matrix computed from these basis functions is the identity matrix:

$$\begin{aligned} (W_{i,j}^{-1/2} Q_{i,j})^T W_{i,j} (W_{i,j}^{-1/2} Q_{i,j}) &= Q_{i,j}^T Q_{i,j} \\ &= I. \end{aligned}$$

The information stored in $R_{i,j}$ can be used to determine the gradient of the orthogonal basis functions. For example, the x and y components of the gradient of the orthonormal basis functions at the volume quadrature points are given by

$$\frac{1}{\Delta x_{i,j}} \frac{\partial V_{i,j}}{\partial \xi} R_{i,j}^{-1}, \text{ and } \frac{1}{\Delta y_{i,j}} \frac{\partial V_{i,j}}{\partial \eta} R_{i,j}^{-1},$$

respectively. In the above formulas, the $1/\Delta x_{i,j}$ and $1/\Delta y_{i,j}$ multipliers are due to the mapping (4.3). Similarly, the values of the basis functions at the surface quadrature points are given by $S_{i,j} R_{i,j}^{-1}$, where $S_{i,j}$ is a Vandermonde-like matrix containing the initial basis functions $\{P_k(\xi, \eta)\}_{k=0,\dots,N_p}$ evaluated at the Gauss-Legendre quadrature points on each edge of $K_{i,j}$ mapped to $[0, 1]^2$ using (4.3).

4.3. Merging neighborhood basis generation. We also need to generate an orthogonal polynomial basis on each merging neighborhood that is orthogonal with respect to the weighted inner product

$$(4.5) \quad \langle f, g \rangle_{\hat{K}_{i,j}} = \frac{1}{|\hat{K}_{i,j}|} \sum_{(r,s) \in M_{i,j}} \frac{1}{N_{r,s}} \int_{K_{r,s}} f g \, dx \, dy,$$

where $N_{r,s}$ is the number of overlapping neighborhoods on cell (r, s) , and

$$|\hat{K}_{i,j}| = \sum_{(r,s) \in M_{i,j}} \frac{|K_{r,s}|}{N_{r,s}},$$

is the weighted volume of the merging neighborhood. The quadrature points at which the merging neighborhood basis is computed are the same quadrature points as the ones used on the cells in base grid (section 2.3). These basis function values are computed by adapting (4.3) to the bounding box of the merging neighborhood. That is, we evaluate $P_k(\xi_{r,s,q}, \eta_{r,s,q})$ at each of the volume quadrature points $(x_{r,s,q}, y_{r,s,q})$ on the merging neighborhood $\hat{K}_{i,j}$, $\forall (r, s) \in M_{i,j}$, using the mapping

$$(4.6) \quad (\xi_{r,s,q}, \eta_{r,s,q}) = \left(\frac{x_{r,s,q} - \hat{x}_{i,j,\min}}{\Delta \hat{x}_{i,j}}, \frac{y_{r,s,q} - \hat{y}_{i,j,\min}}{\Delta \hat{y}_{i,j}} \right)$$

where $(\xi_{r,s,q}, \eta_{r,s,q})$ is again the volume quadrature point $(x_{r,s,q}, y_{r,s,q})$ mapped to $[0, 1]^2$, $\Delta \hat{x}_{i,j}$ is the width of merging neighborhood i, j 's bounding box in the x direction, and $\hat{x}_{i,j,\min}$ is the minimum x

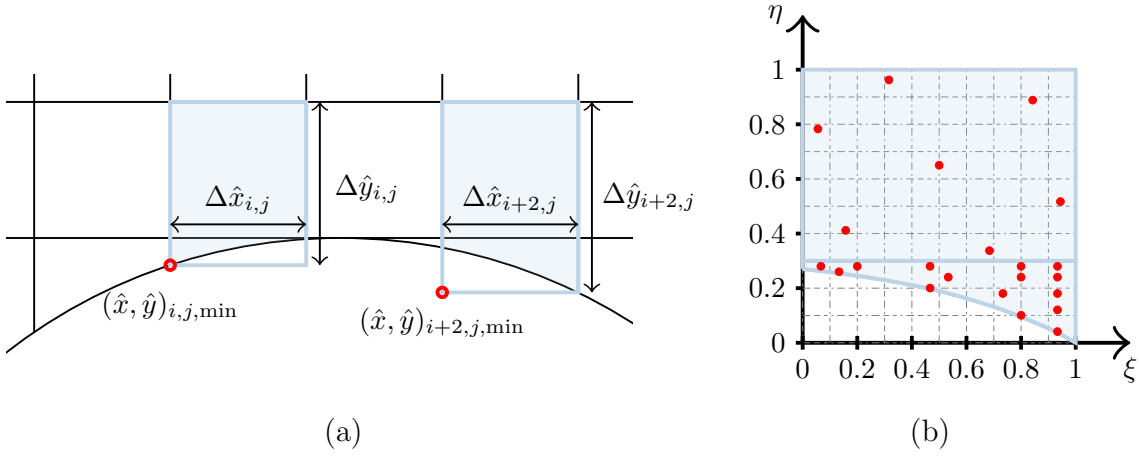


FIG. 4.3. The above figures illustrate how the bounding box of a merging neighborhood is used to generate the neighborhood basis functions. In a), we indicate the bottom left coordinates (•) and dimensions of the bounding box for merging neighborhoods $\hat{K}_{i,j}$ and $\hat{K}_{i+2,j}$ used for the merging basis function calculation on the grid on the top row of Figure 4.1. In b), we plot the points $(\xi, \eta)_{i+2,j,q}$ for $q = 0, 2, \dots$ (indicated by •) at which the basis functions $P_k(\xi, \eta)$ are evaluated to populate the initial Vandermonde-like matrix for merging neighborhood $\hat{K}_{i+2,j}$. Note that the quadrature points on each subelement of the merging neighborhoods are the same as the ones used in section 4.2.

component of all the vertices of $\hat{K}_{i,j}$. $\Delta\hat{y}_{i,j}$ and $\hat{y}_{i,j,\min}$ are similarly defined in the y direction. These quantities are illustrated in Figure 4.3 for two merging neighborhoods on the mesh on the top row of Figure 4.1. We can quickly precompute the merging basis function values using a discrete inner product and a QR factorization, as described in section 4.2. The discrete weighted inner product is given by

$$(4.7) \quad \langle f, g \rangle_{\hat{K}_{i,j}} = \frac{1}{|\hat{K}_{i,j}|} \sum_{(r,s) \in M_{i,j}} \frac{|K_{r,s}|}{N_{r,s}} \sum_{q=0}^{N_{i,j}^{\text{vol}}} w_{r,s,q} f(r_{r,s,q}, s_{r,s,q}) g(r_{r,s,q}, s_{r,s,q}),$$

where $(w_{r,s,q}, x_{r,s,q}, y_{r,s,q})$ are the quadrature weights and points on each cell in the merging neighborhood $(r, s) \in M_{i,j}$, and again $\sum_q w_{r,s,q} = |K_{r,s}|$ and $w_{r,s,q} > 0$ for $q = 0 \dots N_{i,j}^{\text{vol}}$. This basis will be used in the projection operations that stabilize the numerical solution, described in the next section.

5. State redistribution in two dimensions. We are now in a position to describe the state redistribution method on two-dimensional cut cell grids. It is applied after each forward Euler step in a high order SSP-RK time stepper. For non SSP-RK time steppers, the SRD operator can be applied to the intermediate and final solutions. The algorithm follows the operations described in one dimension (section 3), where the numerical solution is provisionally updated, then stabilized by two projection operations. The first projection moves the provisionally updated numerical solution from the base grid onto the merging neighborhoods (section 3, step 1). The second projection moves the merging neighborhood solution back onto the base grid in a conservative manner (section 3, step 2).

To begin, we compute a forward Euler step or an intermediate solution of the RK scheme using the same Δt on all cells, both whole and cut. For example, a forward Euler step for a scalar conservation law is written

$$(5.1) \quad \hat{c}_{i,j,k} = c_{i,j,k}^n - \frac{\Delta t}{|K_{i,j}|} \left[\int_{\partial K_{i,j}} \varphi_{i,j,k} \mathbf{F}^*(U_{i,j}^-, U_{i,j}^+) \cdot \mathbf{n} \, dl - \int_{K_{i,j}} \mathbf{F}(U_{i,j}) \cdot \nabla \varphi_{i,j,k} \, dx \, dy \right],$$

where $\hat{c}_{i,j,k}$ for $k = 0, \dots, N_p$, are the provisionally updated, possibly unstable degrees of freedom, and Δt is the stable time step given by the CFL condition in (2.5).

Next, we project the provisionally updated numerical solution onto the weighted merging basis precomputed in section 4.3, using the discrete weighted inner product (4.7). The solution on the merging basis is

$$\hat{Q}_{i,j}(x) = \sum_{k=0}^{N_p} \hat{q}_{i,j,k} \hat{\varphi}_{i,k}(x, y)$$

where the solution coefficients are

$$(5.2) \quad \hat{q}_{i,j,k} = \frac{1}{|\hat{K}_{i,j}|} \sum_{(r,s) \in M_{i,j}} \frac{1}{N_{r,s}} \int_{K_{r,s}} \hat{\varphi}_{i,j,k} \hat{U}_{r,s} \, dx \, dy,$$

due to the orthogonality of $\hat{\varphi}_{i,j,k}$, and

$$\hat{U}_{r,s}(x) = \sum_{k=0}^{N_p} \hat{c}_{i,j,k} \varphi_{i,j,k}(x, y).$$

Finally, the numerical solution on the neighborhoods is projected back onto the base grid by averaging the overlapping neighborhood solutions:

$$(5.3) \quad c_{i,j,k}^{n+1} = \frac{1}{|K_{i,j}|} \sum_{(r,s) \in W_{i,j}} \frac{1}{N_{i,j}} \int_{K_{i,j}} \varphi_{i,j,k} \hat{Q}_{r,s} \, dx \, dy,$$

where $c_{i,j,k}^{n+1}$ is the stabilized solution coefficient on the base grid, and $W_{i,j}$ is the set of neighborhood indices that overlap cell (i, j) . In the above formula, we average the projection from different, overlapping neighborhoods that contain the same cell in the base grid. As an example, the set of neighborhood indices that overlap $K_{i,j+1}$ in Figure 4.1a) and b) is $W_{i,j+1} = \{(i, j), (i, j+1)\}$. This set does not in fact need to be precomputed and the action of (5.3) can be implemented using a nested for loop (Algorithm 5.1). *Note:* the state redistribution method is a linear operation, so it can be implemented with a simple matrix vector product.

Algorithm 5.1 Implementation of (5.3) without constructing $W_{i,j}$

```

for  $i, j, k$  do
   $c_{i,j,k}^{n+1} \leftarrow 0$ 
end for
for  $i, j$  do
  for  $(r, s) \in M_{i,j}$  do
    for  $k = 0 \dots N_p$  do
       $c_{r,s,k}^{n+1} \leftarrow c_{r,s,k}^{n+1} + (\int_{K_{r,s}} \varphi_{r,s,k} \hat{Q}_{i,j} \, dx \, dy) / (|K_{r,s}| N_{r,s})$ 
    end for
  end for
end for

```

6. Accuracy and conservation. In this section, we show that state redistribution does not modify polynomial solutions to (2.4), or in other words, it is p -exact. We also show that state redistribution is conservative. Similar to finite volume schemes [11], this DG scheme stabilized by state redistribution is not monotone and as a result is not total variation diminishing.

6.1. Claim 1: p -exactness. P -exactness follows from the fact that each step in the state redistribution algorithm preserves polynomials of degree p . Consider the case where the provisionally updated DG solution is a polynomial of degree p on the entire domain $\hat{U}_{i,j}(x, y) = f(x, y)$, with $f \in S^p(\Omega)$, $\forall K_{i,j}$. Projecting the provisionally updated numerical solution onto each weighted merging

basis using the weighted inner product $\langle \cdot, \cdot \rangle_{\hat{K}_{i,j}}$, we have that the solution on all merging neighborhoods is the original function $\hat{Q}_{i,j}(x, y) = f(x, y)$, since the merging basis $\{\hat{\varphi}_{i,j,k}\}_{k=0\dots N_p}$ spans $S^p(\hat{K}_{i,j})$, $\forall K_{i,j}$. Projecting the average of overlapping neighborhood solutions back onto the base grid using the inner product $\langle \cdot, \cdot \rangle_{K_{i,j}}$, the solution in the final update (5.3) remains $U_{i,j}^{n+1}(x, y) = f(x, y)$, since $\text{span}_{k=0\dots N_p}\{\varphi_{i,j,k}\} = S^p(K_{i,j})$, $\forall K_{i,j}$.

6.2. Claim 2: conservation. Conservation follows for the same reason as for the finite volume scheme. We adapt the proof presented in [11] to DG methods. The total mass of the DG numerical solution after one forward Euler step of the RK scheme is

$$\begin{aligned} \mathcal{M}^{n+1} &= \sum_{i,j} \int_{K_{i,j}} U_{i,j}^{n+1}(x, y) \, dx \, dy \\ (6.1) \quad &= \sum_{i,j} |K_{i,j}| c_{i,j,0}^{n+1}, \end{aligned}$$

because $\varphi_{i,j,0} = 1$ and orthogonality of the basis functions. Using the final update (5.3) for the solution coefficient $c_{i,j,0}^{n+1}$ associated to the constant basis function in (6.1), we obtain

$$(6.2) \quad \mathcal{M}^{n+1} = \sum_{i,j} \frac{1}{N_{i,j}} \sum_{(r,s) \in W_{i,j}} \int_{K_{i,j}} \hat{Q}_{r,s} \, dx \, dy.$$

Note that the total mass can also be written as a sum of contributions from each merging neighborhood by rearranging the sum in (6.2), i.e.,

$$(6.3) \quad \mathcal{M}^{n+1} = \sum_{i,j} \hat{\mathcal{M}}_{i,j},$$

where the contribution of merging neighborhood (i, j) is

$$\begin{aligned} \hat{\mathcal{M}}_{i,j} &= \sum_{(r,s) \in M_{i,j}} \frac{1}{N_{r,s}} \int_{K_{r,s}} \hat{Q}_{i,j}(x, y) \, dx \, dy, \\ (6.4) \quad &= |\hat{K}_{i,j}| \langle \hat{Q}_{i,j}, 1 \rangle_{\hat{K}_{i,j}}. \end{aligned}$$

Recognizing that the first equation in (6.4) is the weighted projection of $\hat{Q}_{i,j}(x, y)$ onto the neighborhood's constant basis function $\hat{\varphi}_{i,j,0} = 1$ scaled by $|\hat{K}_{i,j}|$, we have

$$(6.5) \quad \hat{\mathcal{M}}_{i,j} = |\hat{K}_{i,j}| \hat{q}_{i,j,0},$$

Using (5.2) in (6.5), we obtain

$$(6.6) \quad \hat{\mathcal{M}}_{i,j} = \sum_{(r,s) \in M_{i,j}} \frac{1}{N_{r,s}} \int_{K_{r,s}} \hat{U}_{r,s} \, dx \, dy.$$

Substituting the neighborhood contribution (6.6) into the expression for total mass on the grid (6.3), we have

$$(6.7) \quad \mathcal{M}^{n+1} = \sum_{i,j} \sum_{(r,s) \in M_{i,j}} \frac{1}{N_{r,s}} \int_{K_{r,s}} \hat{U}_{r,s} \, dx \, dy.$$

This simplifies to

$$(6.8) \quad \mathcal{M}^{n+1} = \sum_{i,j} \int_{K_{i,j}} \hat{U}_{i,j} \, dx \, dy,$$

and shows that the mass is the same before and after state redistribution.

7. Numerical experiments. In this section, we demonstrate the performance of state redistribution method on a number of test problems. We solve a time-dependent scalar advection problem as well as steady state problems in gas dynamics. In all numerical experiments, we use a time step that is proportional to the size of cells in the background mesh, given by

$$\Delta t \left(\frac{|a|}{\Delta x} + \frac{|b|}{\Delta y} \right) = \frac{0.9}{2p+1},$$

where $|a|$, $|b|$ are the maximum wave speeds in the x and y directions. On all embedded boundary grids, $\Delta x = \Delta y$ and N is the number of cells in each direction. We compute the discrete L_1 and L_∞ errors

$$(7.1) \quad \begin{aligned} L_1 &= \sum_{i,j} \sum_{q=0}^{N_{i,j}^{\text{vol}}} w_{i,j,q} |U_{i,j}(x_{i,j,q}, y_{i,j,q}) - u(x_{i,j,q}, y_{i,j,q})|, \\ L_\infty &= \max_{i,j} \max_q |U_{i,j}(x_{i,j,q}, y_{i,j,q}) - u(x_{i,j,q}, y_{i,j,q})|, \end{aligned}$$

where $U_{i,j}(x, y)$ and $u(x, y)$ are respectively the numerical and exact solutions.

7.1. Solid body rotation. In this example, we solve for the solid body rotation of a pulse around an annulus described in [3, 33]. The conservation law

$$u_t - 0.4\pi[(y - 1.5)u]_x + 0.4\pi[(x - 1.5)u]_y = 0,$$

rotates the initial condition

$$u(x, y, 0) = w(\theta - \pi/2),$$

where

$$w(\theta) = \frac{1}{2} \left[\text{erf}(5(\pi/6 - \theta)) + \text{erf}(5(\pi/6 + \theta)) \right].$$

The initial condition is plotted in Figure 7.2c) on the domain enclosed by two concentric discs of radii $R_1 = 0.75$ and $R_2 = 1.25$. We use the upwind numerical flux and impose zero flow at the boundary, i.e., $\mathbf{F}^* \cdot \mathbf{n} = 0$ at each boundary quadrature point. Figure 7.2a) shows the computational domain embedded on a 50×50 grid. The exact solution is the initial condition rotated about the point $(1.5, 1.5)$, where the final time $T = 5$ corresponds to one solid body rotation. The annulus is embedded on the domain $[0, 3.0001]^2$, where the x and y domain length is slightly perturbed from 3 to prevent cell degeneracies. The minimum volume fraction, $\min_{i,j} |K_{i,j}|/(\Delta x \Delta y)$, in this convergence test is $6.84\text{e-}10$.

In Figure 7.1d) and e), we plot the DG- $P5Q5$ numerical solution on the inner and outer embedded boundaries on a coarse 10×10 grid at the final time. Segments corresponding to different elements are plotted in different colors. We see that there are no glitches or instabilities in the numerical solution on the cut cells.

Discussion of the accuracy. In Figures 7.2b) and d), we provide the L_1 and L_∞ errors in (7.1), respectively. The expected $p + 1$ rate of convergence in the L_1 norm is observed, but the rate of convergence in the L_∞ norm is between p and $p + 1$. This is in contrast to the one-dimensional results in section 3, where the full rate of convergence in both norms was observed. This is the price of automatic mesh generation that we are willing to pay. The nonsmoothness of the error in the L_∞ norm has been observed before and is due to the irregularity of the grid at the cut cells [11, 16]. In [16], it is found that the rate of convergence in L_∞ depends on the geometry of the domain. Here, we find that this rate also depends on the polynomial degree of approximation and varies between p and $p + 1$.

Comparison with finite volume schemes. We compare the numerical solution obtained with our DG scheme to the one obtained with a second order rotated grid h -box method for finite volumes described in [33].

N	FV (h -box [33])	DG- $P1Q1$ (SRD)	DG- $P1Q2$ (SRD)
100	7.50e-02 (-)	4.43e-03 (-)	4.24e-03 (-)
200	2.03e-02 (1.88)	9.17e-04 (2.27)	8.36e-04 (2.34)
400	5.14e-03 (1.98)	2.16e-04 (2.08)	1.90e-04 (2.13)
800	1.29e-03 (1.99)	5.35e-05 (2.01)	4.60e-05 (2.04)

(a) Domain E_d

N	FV (h -box [33])	DG- $P1Q1$ (SRD)	DG- $P1Q2$ (SRD)
100	3.87e-02 (-)	6.73e-03 (-)	3.29e-03 (-)
200	1.01e-02 (1.93)	2.54e-03 (1.40)	1.14e-03 (1.52)
400	2.56e-03 (1.98)	1.01e-03 (1.33)	4.57e-04 (1.31)
800	6.45e-04 (1.99)	4.29e-04 (1.23)	1.77e-04 (1.36)

(b) Outer boundary E_b

N	FV (h -box [33])	DG- $P1Q1$ (SRD)	DG- $P1Q2$ (SRD)
100	1.39e-01 (-)	1.59e-02 (-)	1.49e-02 (-)
200	4.01e-02 (1.79)	5.37e-03 (1.56)	4.39e-03 (1.76)
400	1.02e-02 (1.97)	2.10e-03 (1.35)	1.40e-03 (1.64)
800	2.56e-03 (1.99)	8.78e-04 (1.25)	4.69e-04 (1.58)

(c) Inner boundary E_b

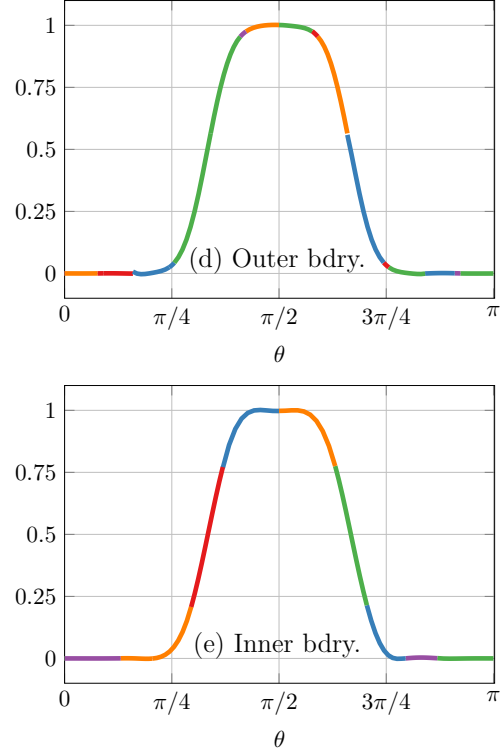


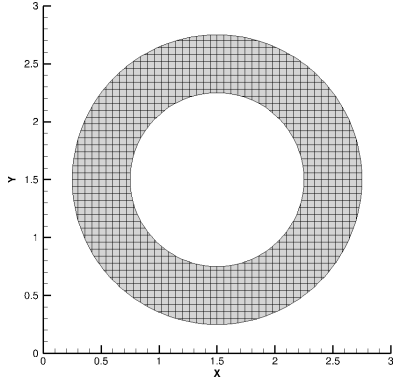
FIG. 7.1. On the left, we compare solutions to the solid body rotation problem in section 7.1 computed with DG- $P1Q1$, DG- $P1Q2$, and FV h -box [33] methods. In a), b), and c) the L_1 errors on the domain, and on the inner and outer boundaries (E_d , E_b) of the numerical solution computed by all three numerical methods are provided, respectively. The errors in the FV column are taken from Table 3.1 of [33], and the numbers in parentheses are the estimated order of convergence. On the right in d) and e), we plot the DG- $P5Q5$ numerical solution on the outer and inner embedded boundary of a 10×10 grid, respectively. Segments corresponding to different elements are plotted in different colors.

In [33], the L_1 error at the final time for second order accurate finite volume methods is measured on the domain interior and boundary using

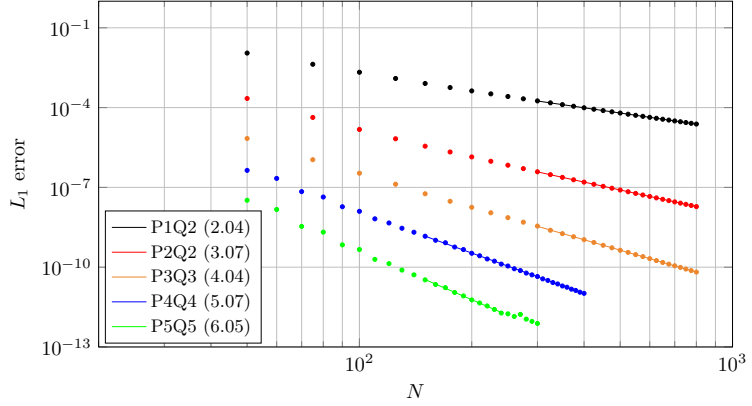
$$(7.2) \quad E_d = \frac{\sum_{i,j} |\bar{U}_{i,j} - u(x_{i,j}, y_{i,j})| |K_{i,j}|}{\sum_{i,j} |u(x_{i,j}, y_{i,j})| |K_{i,j}|} \quad \text{and} \quad E_b = \frac{\sum_{(i,j) \in B} |\bar{U}_{i,j} - u(x_{i,j}, y_{i,j})| |b_{i,j}|}{\sum_{(i,j) \in B} |u(x_{i,j}, y_{i,j})| |b_{i,j}|},$$

respectively, where $(x_{i,j}, y_{i,j})$ are the cell centroids, B is the set of indices of all cells that lie on the domain boundary, and $|b_{i,j}|$ is length of the cut cell's boundary segment. Since second order finite volume methods typically represent curved boundaries with linear segments, we compute the L_1 errors in (7.2) for both DG- $P1Q1$ and DG- $P1Q2$ methods.

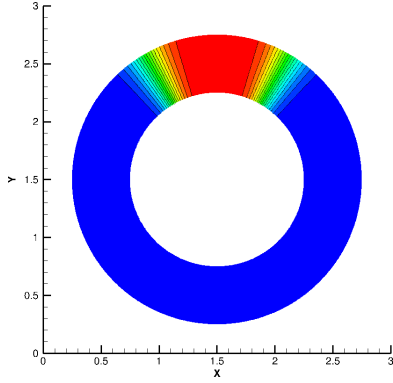
We find that the error is smaller on the outer boundary than on the inner boundary in Figures 7.1b) and c). This agrees with the results in [33], where this phenomenon is attributed to the outer boundary having more cells to resolve the sloped regions of the pulse. As expected, the DG- $P1Q2$ scheme is more accurate than DG- $P1Q1$ scheme due to the higher fidelity representation of the boundary. Additionally, the DG- $P1Q1$ scheme is approximately an order of magnitude more accurate than the FV h -box scheme in Figure 7.1a). The boundary errors of the DG schemes are smaller than the FV ones, although the difference between FV and DG schemes here is not as pronounced. Finally, we observe that the FV scheme is second order accurate at the boundary, while the DG- $P1Q1$ and DG- $P1Q2$ schemes are not.



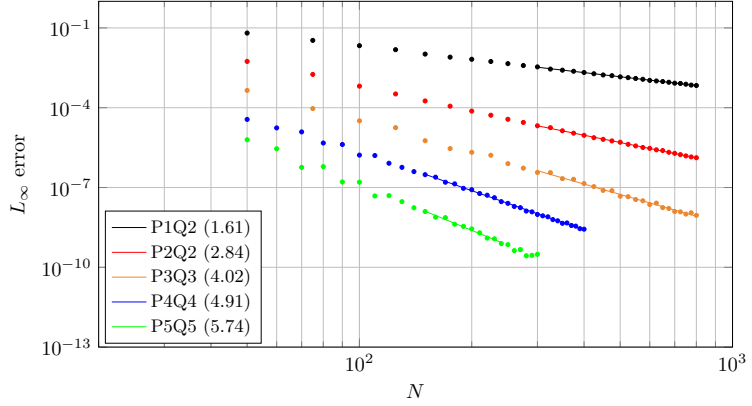
(a)



(b)



(c)



(d)

FIG. 7.2. In a) we plot the annulus domain superimposed on the 50×50 background grid. In c) we plot the isolines of exact solution at the initial and final time. In b) and d) we plot L_1 and L_∞ errors of the solid body rotation problem, respectively. In the legend, we indicate the degree of polynomial approximation on the cells and the boundary segments by P and Q , respectively. The rate of convergence quoted in parentheses is computed by a least squares fit, plotted with a straight line. We observe the expected $p+1$ rate of convergence in the L_1 norm, and a rate of convergence between p and $p+1$ in the L_∞ norm. Additionally, the error in the L_∞ norm is noisy, due to the irregularity of the grid at the cut cells.

7.2. Ringleb flow. In this example, we solve for smooth transonic flow through a curved channel. This test problem is useful to evaluate the accuracy of high order methods with curved boundaries [34, 35, 36, 37, 38]. The exact solution at a given point (x, y) is computed by solving

$$\left(x - \frac{J}{2} - s_x\right)^2 + (y - s_y)^2 = \frac{1}{4\rho^2 k^4},$$

for the speed of sound c using the method of bisection, where

$$\begin{aligned} J &= \frac{1}{c} + \frac{1}{3c^3} + \frac{1}{5c^5} - \frac{1}{2} \ln\left(\frac{1+c}{1-c}\right), \\ q &= \sqrt{\frac{2(1-c^2)}{\gamma-1}}, \quad k = \sqrt{\frac{2}{1/q^2 - 2\rho(x - J/2 - s_x)}}, \\ \rho &= c^{2/(\gamma-1)}, \end{aligned}$$

$\gamma = 1.4$, and ρ, q are the density and speed of the gas, respectively. Additionally, $(s_x, s_y) = (1.5, 0)$ are shifts to center the channel on the domain. The pressure, and x, y components of the flow velocity are given by

$$P = \frac{c^2 \rho}{\gamma}, \quad u = \sqrt{q^2 - v^2}, \quad \text{and} \quad v = \frac{q^2}{k},$$

respectively. The boundaries of the channel are embedded on $[0, 2.75]^2$, and are given by the curves

$$\begin{aligned} x(k, q) &= \frac{1}{2\rho} \left(\frac{1}{q^2} - \frac{2}{k^2} \right) + \frac{J}{2} + s_x, \\ y(k, q) &= \frac{1}{kq\rho} \sqrt{1 - \frac{q^2}{k^2}} + s_y. \end{aligned}$$

The reflecting walls are described by $k = 0.7$ and $k = 1.2$, while the top boundary is described by $q = 0.5$. The domain and exact solution are shown in Figure 7.4a) and c). The exact solution is used as the initial condition, and as the ghost states at the top and bottom boundaries. Roe's numerical flux is used on the interior element interfaces, and the flux on the reflecting walls is given by

$$(7.3) \quad \mathbf{F}^* \cdot \mathbf{n} = \begin{pmatrix} 0 \\ Pn_x \\ Pn_y \\ 0 \end{pmatrix},$$

where $\mathbf{n} = (n_x, n_y)$ is the outward facing normal and P is the internal pressure at the boundary at each quadrature point. The solver is run until the stopping criterion

$$(7.4) \quad \max_{i,j} \|\mathbf{c}_{i,j}^{n+1} - \mathbf{c}_{i,j}^n\|_\infty < 10^{-13}$$

is satisfied. The minimum volume fraction, $\min_{i,j} |K_{i,j}|/(\Delta x \Delta y)$, in this convergence test is 1.25e-09.

This test case is interesting for two reasons. First, the flow smoothly transitions from subsonic to supersonic and the Mach number reaches an approximate maximum of 1.42 near the bottom right corner of the domain. Second, the embedded boundary presents sharp corners. The cut cells on which these corners lie may not have a unique normal merging neighborhood. For example, in Figure 7.3a), the cut cell on the top left corner of the domain can either be merged downward or to the right. Instead of choosing one of the two possible normal merging neighborhoods, we use the 3×3 central merging neighborhood, shown in Figure 7.3b). We do this for the cut cells at the top left and right corners of the domain, which result in higher overlap counts.

We provide the L_1 and L_∞ errors in the entropy in Figure 7.4b) and d), where the entropy is given by P/ρ^γ . We observe the expected $p+1$ rate of convergence in the L_1 norm and a rate between p and $p+1$ in the L_∞ norm. This test problem was solved in [34], where their spectral volume scheme on unstructured triangles may form shocks that do not allow convergence of the method. For all meshes considered here, our solver converged and the stopping criterion (7.4) was attained. Finally, in [39] a second order finite volume method solved a similar Ringleb flow problem on cut cell grids, and observed a rate of convergence of 2.02 in L_1 and 1.40 in L_∞ .

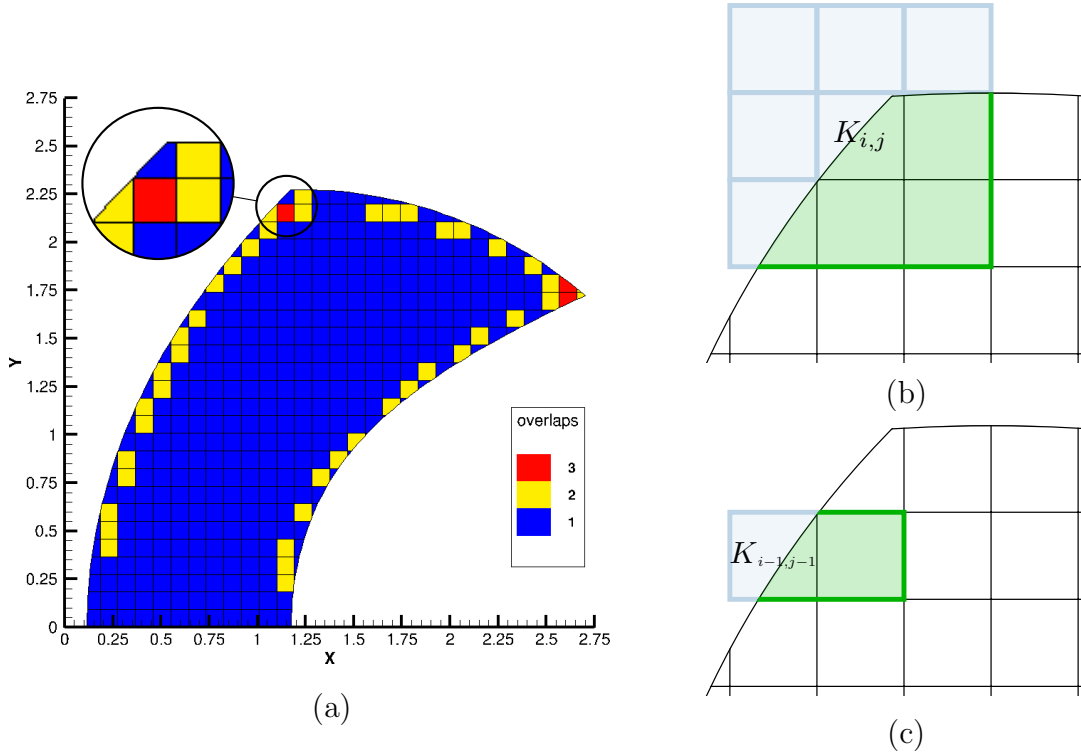


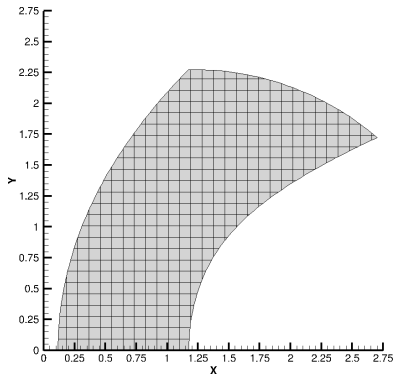
FIG. 7.3. In a), we plot the overlap counts of the Ringleb domain on the 30×30 grid. On most cut cells, we use the normal merging neighborhood. When the volume constraint (4.1) cannot be satisfied, or there is a corner on the cut cell, we use the 3×3 central merging neighborhood. This is illustrated with the neighborhood associated to $K_{i,j}$ in b), which overlaps with the neighborhood associated to $K_{i-1,j-1}$ shown in c). In both b) and c), the cells highlighted in green are the merging neighborhoods and the portions that are highlighted in blue are solid and do not belong to the computational grid. The highlighted red cell in a), $K_{i,j-1}$, is overlapped by three neighborhoods: $\hat{K}_{i,j}$, $\hat{K}_{i-1,j-1}$, and $\hat{K}_{i,j-1}$.

7.3. Scattering of a smooth pressure pulse. In this example, we compute the scattering of a pressure pulse surrounded by five circular obstacles. The computational domain is $[0, 20]^2$ and the obstacles are centered at $(10 + 5 \cos(\varphi_k), 10 + 5 \sin(\varphi_k))$ for $\varphi_k = 2\pi k/5 - 2\pi/3$. The initial condition is given by

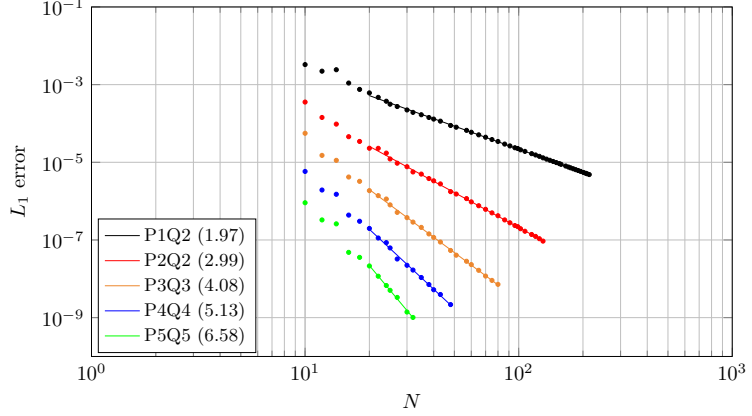
$$\begin{pmatrix} \rho \\ u \\ v \\ P \end{pmatrix} = \begin{pmatrix} 1 - 1/\gamma + P \\ 0 \\ 0 \\ 1/\gamma + 10^{-4} \exp(-b[(x-10)^2 + (y-10)^2]) \end{pmatrix},$$

where $\gamma = 1.4$, $b = \log(2)/0.2^2$, and the disturbance in the pressure is a Gaussian located at $(10, 10)$. The domain is discretized into a 53×53 cut cell grid, where each boundary segment is a polynomial of degree five ($q = 5$). On this grid, the minimum volume fraction, $\min_{i,j} |K_{i,j}|/(\Delta x \Delta y)$, is $7.28\text{e-}06$. Roe's numerical flux is used on the interior element interfaces, the flux along the reflecting obstacles is given by (7.3), and the ghost state on the outer boundaries of the domain is set to quiescent gas, $\rho = 1$, $p = 1/\gamma$, and $u = v = 0$.

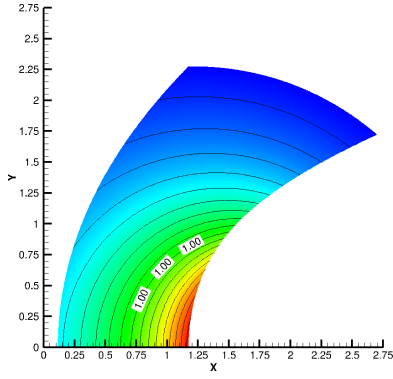
We provide the DG- $P5Q5$ numerical solution at the final time, $T = 6$ in Figure 7.5a) and c), respectively. The solution presents the same five-fold symmetry as the obstacles. The solution along the obstacle indicated by \times is plotted in Figures 7.5b) and d), where we observe sub-cell resolution of the complex scattering phenomenon.



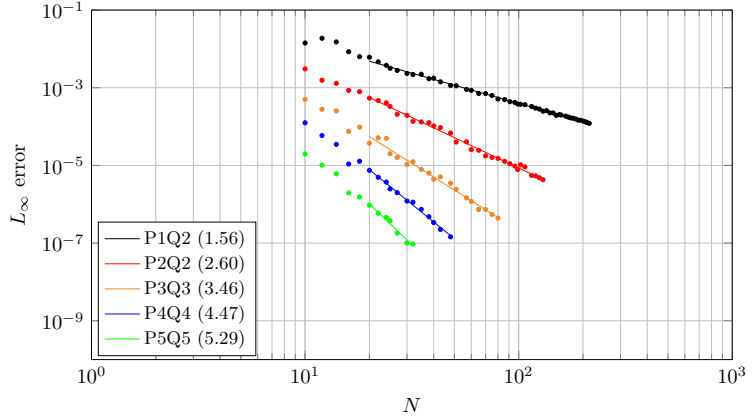
(a)



(b)



(c)



(d)

FIG. 7.4. In a) we plot the Ringleb domain superimposed on a 30×30 background grid. In c) we plot the Mach isolines of the exact solution, where the sonic line is labeled. In b) and d) we plot L_1 and L_∞ entropy errors, respectively. In the legend, we indicate the degree of polynomial approximation on the cells and the boundary segments by P and Q , respectively. The rate of convergence quoted in parentheses is computed by a least squares fit, plotted with a straight line.

8. Conclusions. We have presented a state redistribution method for discontinuous Galerkin methods on curvilinear embedded boundary grids. This technique preserves the formal order of accuracy of the base DG scheme and is conservative. The advantage of state redistribution is that it only uses basic mesh information that is already available in many cut cell codes and does not require complex geometric computations. Numerical examples reveal that the order of accuracy of the DG scheme is $p+1$ in the L_1 norm and between p and $p+1$ in L_∞ . We find that rate in L_∞ depends on the problem, the geometry of the embedded boundary, as well as the polynomial degree of approximation p . This is a price that we are willing to pay in exchange for automatic mesh generation. Future work includes studying more closely the loss of accuracy at the boundary and attempt to improve it. We will also extend the method to three dimensions and more realistic engineering geometries. In particular, we will have to consider severely ill-shapen cut cells that commonly occur in three dimensions. Finally, when we extend our method to viscous flows, we would like to adapt state redistribution to the Navier-Stokes equations.

9. Code availability. We have made a one-dimensional DG-SRD implementation in Python available at <https://github.com/andrewgiuliani/PyDGSRD-1D>. This code will reproduce the convergence

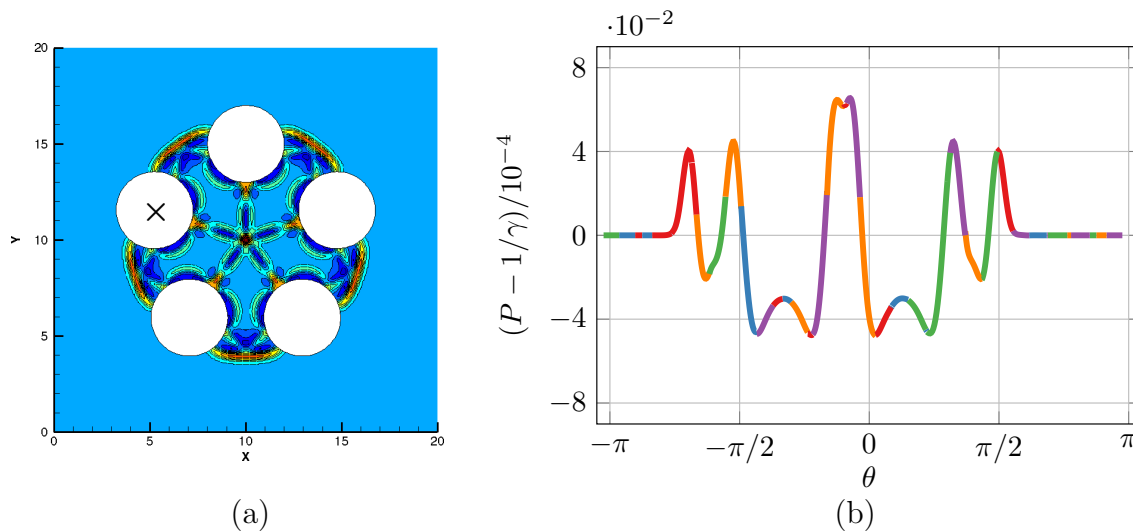


FIG. 7.5. In a), we plot the scaled deviation from the mean pressure, $(P - 1/\gamma)/10^{-4}$, at the final time. In b), we provide this pressure deviation along the obstacle indicated by a \times . Segments corresponding to different elements are plotted in different colors. We observe that the numerical solution retains the five-fold symmetry of the domain. On the embedded boundary, we observe the complex variation of the pressure in the scattered pulse.

test in section 3 and can be applied to other conservation laws on nonuniform grids. We have also made our cut cell mesh generation code written in Python available at <https://github.com/andrewgiuliani/PyGrid-2D>. This code can be used to reproduce all the grids used in the numerical experiments in section 7, as well as generate other high order embedded boundary grids in two dimensions.

10. Acknowledgements. The author would like to thank Marsha Berger, Sandra May, Georg Stadler, and Lilia Krivodonova for their reading of the manuscript and helpful comments. We would also like to thank Marco Vianello for the helpful discussions on using the quadrature rule generation code. AG is partially supported by the Natural Sciences and Engineering Research Council of Canada (NSERC) under Award No. PDF-546085-2020 and by the Simons Foundation/SFARI (560651, AB).

REFERENCES

- [1] J. Dongarra, J. Hittinger, J. Bell, L. Chacon, R. Falgout, M. Heroux, P. Hovland, E. Ng, C. Webster, and S. Wild, “Applied mathematics research for exascale computing,” tech. rep., Lawrence Livermore National Lab, 2 2014.
- [2] P. Colella, D. T. Graves, B. J. Keen, and D. Modiano, “A Cartesian grid embedded boundary method for hyperbolic conservation laws,” *Journal of Computational Physics*, vol. 211, no. 1, pp. 347–366, 2006.
- [3] M. Berger and C. Helzel, “A simplified h-box method for embedded boundary grids,” *SIAM J. Sci. Comput.*, vol. 34, 2012.
- [4] C. Helzel, M. Berger, and R. LeVeque, “A high-resolution rotated grid method for conservation laws with embedded geometries,” *SIAM J. Sci. Comput.*, vol. 26, pp. 785–809, 2005.
- [5] S. Jebens, O. Knöth, and R. Weiner, “Linearly implicit peer methods for the compressible Euler equations,” *Applied Numerical Mathematics*, vol. 62, no. 10, pp. 1380 – 1392, 2012. Selected Papers from NUMDIFF-12.
- [6] S. May and M. Berger, “An explicit implicit scheme for cut cells in embedded boundary meshes,” *J. Sci. Comput.*, 2016.
- [7] R. Klein, K. Bates, and N. Nikiforakis, “Well-balanced compressible cut-cell simulation of atmospheric flow,” *Philosophical Transactions of the Royal Society A: Mathematical, Physical and Engineering Sciences*, vol. 367, no. 1907, pp. 4559–4575, 2009.
- [8] N. Gokhale, N. Nikiforakis, and R. Klein, “A dimensionally split Cartesian cut cell method for hyperbolic conservation laws,” *Journal of Computational Physics*, vol. 364, pp. 186–208, 2018.
- [9] J. J. Quirk, “An alternative to unstructured grids for computing gas dynamic flows around arbitrarily complex two-dimensional bodies,” *Computers & fluids*, vol. 23, no. 1, pp. 125–142, 1994.
- [10] S. Xu, T. Aslam, and D. Stewart, “High resolution numerical simulation of ideal and non-ideal compressible reacting

- flows with embedded internal boundaries,” *Combustion Theory and Modelling*, vol. 1, no. 1, pp. 113–142, 1997.
- [11] M. Berger and A. Giuliani, “A state redistribution algorithm for finite volume schemes on cut cell meshes,” *Journal of Computational Physics*, vol. 428, p. 109820, 2021.
 - [12] R. Qin and L. Krivodonova, “A discontinuous Galerkin method for solutions of the Euler equations on Cartesian grids with embedded geometries,” *Journal of Computational Science*, vol. 4, no. 1, pp. 24 – 35, 2013. Computational Methods for Hyperbolic Problems.
 - [13] S. Schoeder, S. Sticko, G. Kreiss, and M. Kronbichler, “High-order cut discontinuous Galerkin methods with local time stepping for acoustics,” *International Journal for Numerical Methods in Engineering*, vol. 121, no. 13, pp. 2979–3003, 2020.
 - [14] D. Krause and F. Kummer, “An incompressible immersed boundary solver for moving body flows using a cut cell discontinuous Galerkin method,” *Computers & Fluids*, vol. 153, pp. 118–129, 2017.
 - [15] B. Müller, S. Krämer-Eis, F. Kummer, and M. Oberlack, “A high-order discontinuous Galerkin method for compressible flows with immersed boundaries,” *International Journal for Numerical Methods in Engineering*, vol. 110, no. 1, pp. 3–30, 2017.
 - [16] C. Engwer, S. May, A. Nüßing, and F. Streitbürger, “A stabilized DG cut cell method for discretizing the linear transport equation,” *SIAM Journal on Scientific Computing*, vol. 42, no. 6, pp. A3677–A3703, 2020.
 - [17] K. J. Fidkowski and D. L. Darmofal, “A triangular cut-cell adaptive method for high-order discretizations of the compressible Navier–Stokes equations,” *Journal of Computational Physics*, vol. 225, no. 2, pp. 1653 – 1672, 2007.
 - [18] K. Fidkowski and D. Darmofal, “An adaptive simplex cut-cell method for discontinuous Galerkin discretizations of the Navier-Stokes equations,” in *18th AIAA Computational Fluid Dynamics Conference*, p. 3941, 2007.
 - [19] F. Bassi and S. Rebay, “High-order accurate discontinuous finite element solution of the 2D Euler equations,” *Journal of Computational Physics*, vol. 138, no. 2, pp. 251–285, 1997.
 - [20] B. Cockburn and C.-W. Shu, “The Runge–Kutta discontinuous Galerkin method for conservation laws V: Multidimensional systems,” *Journal of Computational Physics*, vol. 141, no. 2, pp. 199 – 224, 1998.
 - [21] R. Qin and L. Krivodonova, “Spectrum of the discontinuous Galerkin spatial discretization for two dimensional problems,” *Preprint*, 2020.
 - [22] Y. Sudhakar, J. M. De Almeida, and W. A. Wall, “An accurate, robust, and easy-to-implement method for integration over arbitrary polyhedra: application to embedded interface methods,” *Journal of Computational Physics*, vol. 273, pp. 393–415, 2014.
 - [23] B. Müller, F. Kummer, and M. Oberlack, “Highly accurate surface and volume integration on implicit domains by means of moment-fitting,” *International Journal for Numerical Methods in Engineering*, vol. 96, no. 8, pp. 512–528, 2013.
 - [24] F. Kummer, “Extended discontinuous Galerkin methods for two-phase flows: the spatial discretization,” *International Journal for Numerical Methods in Engineering*, vol. 109, no. 2, pp. 259–289, 2017.
 - [25] S. Mousavi, H. Xiao, and N. Sukumar, “Generalized Gaussian quadrature rules on arbitrary polygons,” *International Journal for Numerical Methods in Engineering*, vol. 82, no. 1, pp. 99–113, 2010.
 - [26] R. Saye, “High-order quadrature methods for implicitly defined surfaces and volumes in hyperrectangles,” *SIAM Journal on Scientific Computing*, vol. 37, no. 2, pp. A993–A1019, 2015.
 - [27] A. Sommariva and M. Vianello, “Computing Tchakaloff-like cubature rules on spline curvilinear polygons,” *Dolomites Research Notes on Approximation*, vol. 14, no. 1, 2021.
 - [28] A. Sommariva and M. Vianello, “Matlab codes for computing low cardinality algebraic cubature rules on spline curvilinear polygons.” <https://www.math.unipd.it/~alvise/software.html>.
 - [29] M. Berger, “A note on the stability of cut cells and cell merging,” *Applied Numerical Mathematics*, vol. 96, pp. 180 – 186, 2015.
 - [30] F. Bassi, L. Botti, A. Colombo, D. A. Di Pietro, and P. Tesini, “On the flexibility of agglomeration based physical space discontinuous Galerkin discretizations,” *Journal of Computational Physics*, vol. 231, no. 1, pp. 45–65, 2012.
 - [31] L. Mascotto, “Ill-conditioning in the virtual element method: Stabilizations and bases,” *Numerical Methods for Partial Differential Equations*, vol. 34, no. 4, pp. 1258–1281, 2018.
 - [32] B. R. Lowery and J. Langou, “Stability analysis of QR factorization in an oblique inner product,” *arXiv preprint arXiv:1401.5171*, 2014.
 - [33] C. Helzel, M. J. Berger, and R. J. Leveque, “A high-resolution rotated grid method for conservation laws with embedded geometries,” *SIAM Journal on Scientific Computing*, vol. 26, no. 3, pp. 785–809, 2005.
 - [34] Z. Wang and Y. Liu, “Extension of the spectral volume method to high-order boundary representation,” *Journal of Computational Physics*, vol. 211, no. 1, pp. 154 – 178, 2006.
 - [35] M. Dumbser, M. Käser, V. A. Titarev, and E. F. Toro, “Quadrature-free non-oscillatory finite volume schemes on unstructured meshes for nonlinear hyperbolic systems,” *Journal of Computational Physics*, vol. 226, no. 1, pp. 204 – 243, 2007.
 - [36] P. Houston and N. Sime, “Automatic symbolic computation for discontinuous Galerkin finite element methods,” *SIAM Journal on Scientific Computing*, vol. 40, no. 3, pp. C327–C357, 2018.
 - [37] Z. J. Wang, K. Fidkowski, R. Abgrall, F. Bassi, D. Caraeni, A. Cary, H. Deconinck, R. Hartmann, K. Hillewaert, H. T. Huynh, *et al.*, “High-order CFD methods: current status and perspective,” *International Journal for Numerical Methods in Fluids*, vol. 72, no. 8, pp. 811–845, 2013.
 - [38] L. Ivan and C. P. Groth, “High-order solution-adaptive central essentially non-oscillatory (CENO) method for viscous

- flows,” *Journal of Computational Physics*, vol. 257, pp. 830 – 862, 2014.
- [39] W. J. Coirier and K. G. Powell, “An accuracy assessment of Cartesian-mesh approaches for the Euler equations,” *Journal of Computational Physics*, vol. 117, no. 1, pp. 121–131, 1995.